SEDIMENTOLOGY the journal of the International Association of Sedimentologists

Sedimentology (2021) **68**, 1137–1158 doi: 10.1111/sed.12821

Particle-scale characterization of volcaniclastic dust sources within Iceland

TAMAR RICHARDS-THOMAS, CHERYL MCKENNA-NEUMAN and IAN M. POWER

School of the Environment, Trent University, 1600 West Bank Drive, Peterborough, Ontario, K9L 0G2, Canada (E-mail: trichards@trentu.ca)

Associate Editor – Adam McArthur

ABSTRACT

Volcaniclastic dust particles are characterized by unique physical properties, which are speculated to influence their rates of entrainment, emission and deposition within the atmospheric boundary layer. Few detailed particle-scale measurements exist, so that natural particles often are idealized as solid glass spheres in the parameterization of dust dispersion models. This study shows that volcaniclastic dust particles from Iceland contain substantial quantities of amorphous glass, large internal voids and copious dustcoats comprised of nano-scale flakes. Their high porosity, found to increase with particle diameter, generates particle densities that can be substantially lower than expected for a solid sphere. An abundance of volcanic glass also seems to increase particle porosity and roughness, and thereby strongly correlates with the Brunauer Emmett Teller surface area. An analysis based on Stokes' law further suggests that Icelandic dust with a standardized geometric diameter (10 μm or PM_{10}), but with varying density, shape and origin, may have settling velocities in still air that are up to 20% lower than for a reference glass sphere. As a first approximation, neglecting complex particle interactions and wind speed, which also affect the deposition rate in the atmosphere, their low density and large surface area could increase the expected residence time by a factor of five. Model parameterization should be refined to incorporate these particle-scale factors in order to improve on the estimation of volcaniclastic dust dispersion.

Keywords Iceland, mineralogy, particle size and morphology, specific surface area, volcaniclastic dust.

INTRODUCTION

Iceland is a major high latitude (63 to 67°N) dust source located just below the Arctic Circle (Fig. 1). Volcaniclastic sandy deserts with active aeolian processes, which make up more than 19% (>20 000 km^2) of the surficial geology, contain sediments from both glaciofluvial systems and volcanic eruptions (Arnalds *et al.*, 2001a; Arnalds *et al.*, 2016). The source regions for particulate matter (PM) within Iceland are extremely windy, sparsely vegetated and have little to no gravel pavement to reduce wind erosion, thereby creating favourable conditions for dust storm generation (Einarsson, 1984; Arnalds *et al.*, 2001b; Bullard *et al.*, 2016). Persistent dust sources in Iceland are areas where fresh volcanic ash materials are often deposited from eruptions (Arnalds *et al.*, 2016) in which resuspension of ash leads to longer residence time as compared with ash deposited on glaciers and vegetation (Arnalds, 2010; Thorsteinsson *et al.*, 2011, 2012; Arnalds *et al.*, 2016; Butwin *et al.*, 2019). For instance, frequent volcanic eruptions

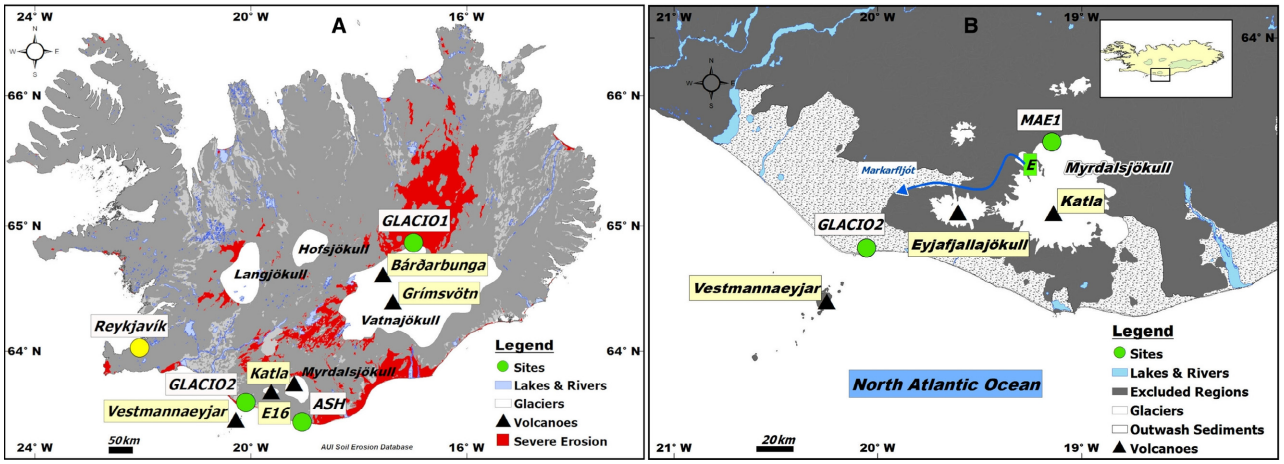

Fig. 1. Sample collection sites located within dust hot spots in Iceland include: (A) Vík (Ash), Dyngjusandur (Glacio1) and Markarfljótsaurar (Glacio2) (Arnalds *et al.*, 2016); (B) Glacio2 sediments are transported from Entujökull (E) located at the outlet of Katla glacier and Mýrdalsjökull to Markarfljótsaurar in southern Iceland. MAE1 refers to fine particulate matter (≤10 μm) collected at the Mælifellssandur dust hot spot (2013; Dagsson-Waldhauserova *et al.*, 2014a), and E16 refers to Eyjafjallajökull volcano.

and re-suspension of volcanic materials led to an annual average of 135 days, where suspended solid particulates were observed in Iceland (Dagsson-Waldhauserová *et al.*, 2014b).

An estimated 31 to 40 Tg of volcanic dust is emitted annually into the atmosphere (Arnalds *et al.*, 2014). The magnitude and frequency of Icelandic dust storms (Thorsteinsson *et al.*, 2011; Prospero *et al.*, 2012; Arnalds *et al.*, 2013; Dagsson-Waldhauserová *et al.*, 2014b) are projected to increase with global warming as glacier retreat exposes new volcanic dust sources (Cannone *et al.*, 2008). Re-suspension of ash from the 2010 Eyjafjallajökull eruption is reported to have increased dust storm frequency (Thorsteinsson *et al.*, 2012; Bullard *et al.*, 2016) and is linked to poor air quality and respiratory health problems in the city of Reykjavík, where more than 80% of the population resides (Thorsteinsson *et al.*, 2011; Carlsen *et al.*, 2015; Fig. 2C). The study of Horwell *et al.* (2013) suggests that the inhalation of angular, blocky Icelandic ash particulates <10 μm (PM_{10}) can lead to respiratory health problems. The deposition of 2010 Eyjafjallajökull ash onto glacier surfaces is observed to reduce the ice albedo (Wittmann *et al.*, 2017; Boy *et al.*, 2019) and, through positive feedback (Boy *et al.*, 2019), exacerbate their retreat.

It is widely speculated that the geometry (size, shape and density) and porosity of volcanic dust particles influence their susceptibility to aeolian entrainment, transport and deposition, yet few *in situ* measurements exist to either test this hypothesis or support the parameterization of dust dispersion models. In theory, particle size, shape, density, porosity and surface area should all be interlinked, thereby affecting dust entrainment, dispersion and deposition rates (Chepil, 1951; Robock, 2000; Riley *et al.*, 2003; Richards-Thomas & McKenna-Neuman, 2020) through variation in fluid drag and gravitational force. Butwin *et al.* (2020) suggest that the low density of large volcanic dust particles may influence their entrainment, suspension and transport over long distances. Indeed, Olsson *et al.* (2013) found that the specific surface areas of particles collected from ash plume fallout increase with growing distance from an eruption's caldera. The large specific surface area of volcanic dust particles upon suspension and transport in the atmosphere could also act as carriers for atmospheric gases and chemicals to attach (Oberdörster, 2001), thereby altering the particle aerodynamic behaviour.

Ash particles up to 70 μm in diameter from the Eyjafjallajökull 2010 eruption were detected by satellite over Europe, about 2000 km from their source (Stevenson *et al.*, 2012); although Pye (1987) and Duce (1995) suggest that the largest expected diameter of a siliciclastic particle suspended in long range transport is much smaller at only 20 μm in diameter. Ash particles up to nine times (180 μm) the diameter of

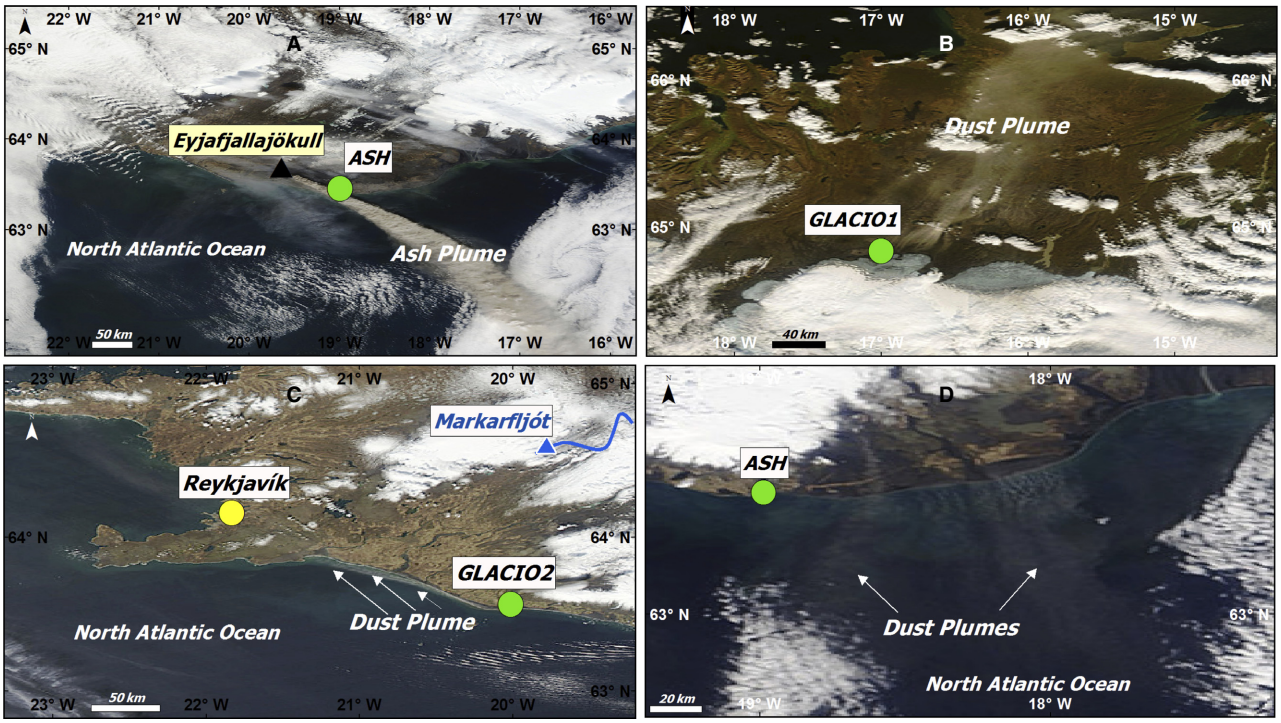

Fig. 2. Examples of satellite images showing the trajectories of dust plumes originating from volcanic dust regions in north-east and southern Iceland. (A) Dust plume from Eyjafjallajökull volcano blowing southeast towards the North Atlantic Ocean on 8 May 2010. (B) Large dust plume blowing *ca* 200 km from Dyngjusandur towards the Arctic on 17 September 2009. (C) Dust plume along the southern coast blowing from regions near Markarfljótsaurar towards the capital city of Reykjavík on 28 April 2007. (D) Multiple dust plumes blowing from the southern region towards the Northern Atlantic Ocean on 23 April 2017. All images were retrieved from NASA Goddard Space Flight Center, LANCE Rapid Response MODIS Terra satellite and labelled in ArcGIS.

siliciclastic particles were also transported over 100 km from the 2011 Grímsvötn eruption (Butwin *et al.*, 2020; and references within). However, Gislason *et al.* (2011; and references within) associate such transport with high particle porosity, which is a key factor to consider when examining the transport of Icelandic dust particles. Indeed, modelling the fate of angular, porous particles in cold, humid environments presents numerous challenges that are not satisfied with current model scheme parameterizations (Del Bello *et al.*, 2018; Richards-Thomas & McKenna-Neuman, 2020).

In the context of the present study, particle size, shape, density, porosity, surface area and mineralogy are measured and compared for sediments collected from several Icelandic sites that are known to experience severe wind erosion, and thereby eject large amounts of dust into the atmospheric boundary Layer (ABL). Secondary objectives include: (i) performance evaluation of several cutting-edge technologies used to characterize the physical properties of these complex aerosols; and (ii) approximation of the dynamical effects of the particle morphology, relative to a solid glass sphere of similar geometric diameter.

Sample origin

Samples were collected from three different source regions for volcaniclastic dust in Iceland (Fig. 1A): Vík, Markarfljótsaurar and Dyngjusandur, the latter site pertaining to a dust hot spot in north-east Iceland (Arnalds *et al.*, 2016).

Freshly deposited 2010 Eyjafjallajökull ash was collected in Vík, 38 km south-east of the volcano, on 6 June 2010 (Richards-Thomas & McKenna-Neuman, 2020), weeks after a phase of the explosive eruption that began on 14 April. Melting of large amounts of glacial ice caused widespread flooding, while interaction of the magma with the

water produced a plume of volcanic ash that extended up to 10 km in elevation as it moved out over the North Atlantic Ocean (Fig. 2A). Over the course of this cyclical eruption event, which persisted into late May, approximately 10 million tonnes of fine particles (2.8 μm < d < 28 μm) were ejected through the troposphere and into the stratosphere (Gislason *et al.*, 2011; Schumann *et al.*, 2011; Stohl *et al.*, 2011). The prevailing atmospheric conditions transported the Eyjafjallajökull ash directly towards Europe, causing the airspace to shut down for a period lasting up to seven consecutive days (Gislason *et al.*, 2011; Horwell *et al.*, 2013).

One month following the 2010 Eyjafjallajökull eruption, a ten-minute average PM concentration of resuspended ash measured in the city of Reykjavík exceeded 2000 μg m^{-3} (Thorsteinsson *et al.*, 2012). However, models are not able to adequately incorporate such resuspension events because the particle residence time is unknown (Butwin *et al.*, 2020). During the eruption, dispersion model performance was undermined by a dearth of information concerning various particle parameters relating to size, shape, density and mineralogy, which would be needed to attain suitable accuracy in calculating the dust deposition rate (Johnson *et al.*, 2012; Leadbetter *et al.*, 2012; Wiegner *et al.*, 2012; Bagheri *et al.*, 2015).

Glaciogenic sediments were collected from the dust hot spot, Dyngjusandur (Glacio1) located north of Vatnajökull glacier in north-east Iceland in 2015, and from Markarfljótsaurar (Glacio2) located west of Mýrdalsjökull and Eyjafjallajökull (E16) glaciers in southern Iceland (Fig. 1). Two kilograms of volcanic dust collected in May 2015 from Dyngjusandur was also used to conduct this study. Dyngjusandur is the largest and one of the most active source regions for volcaniclastic dust in Iceland (Arnalds *et al.*, 2001a; Baratoux *et al.*, 2011), transporting dust particles towards the North Atlantic Ocean (Dagsson-Waldhauserová *et al.*, 2013; Moroni *et al.*, 2018; Fig. 2B) and onto Greenland glaciers (Drab *et al.*, 2002; Meinander *et al.*, 2016). A comprehensive description of this site is provided in the earlier studies of Arnalds (2010) and Arnalds *et al.* (2016). Resuspended volcanic dust transported from Dyngjusandur may also influence marine biota within ecosystems in the Arctic Ocean (Dagsson-Waldhauserová *et al.*, 2017), and similarly from Southern Iceland into the Northern Atlantic Ocean (for example, Fig. 2D).

Fifteen kilograms of volcaniclastic dust was also collected from Markarfljótsaurar in September 2016. The volcaniclastic dust source at Markarfljótsaurar originates from frequent catastrophic meltwater floods (jökulhlaup) on the Markarfljöt river from the glacial terminus of Entujökull that are triggered by the interactions between the Mýrdalsjökull glacier and Katla volcano (Smith & Dugmore, 2006; Fig. 1B). Prevailing wind conditions occasionally direct the dust emitted from Markarfljótsaurar towards Reykjavík (Dagsson-Waldhauserová *et al.*, 2016; Mockford *et al.*, 2018; Fig. 2C) where the associated poor air quality has increased respiratory health problems among its residents (Horwell, 2007; Carlsen *et al.*, 2015).

METHODOLOGY

In pre-treatment, each of the three volcanic dust samples was individually: (i) wet sieved (62 μm mesh) in order to isolate the volcaniclastic dust particles; (ii) dried for 24 h at 110°C; and then (iii) mixed vigorously to homogenize the sample and reduce aggregation. The sieve was thoroughly cleaned after each use to prevent the cross-contamination of samples and regularly checked for damage and clogged openings. A laser diffraction particle-size analyzer (LPSA, Horiba-Partica LA-950 V2; Horiba, Kyoto, Japan) verified that over 90% of the wet-sieved particles collected had diameters ≤50 μm. The processed samples were stored inside a desiccator pending further analyses as listed in Table 1, the details of which are provided in the following sections.

Particle imaging

In preparation for imaging with a Hitachi S4500 field emission scanning electron microscope (SEM; Hitachi, Tokyo, Japan) operating at an accelerating voltage of 20 kV, sub-samples were first spread onto separate carbon conductive adhesive tapes mounted on aluminum stubs and then coated with 5 nm osmium to reduce charging effects. The SEM images (2351 by 595 pixels, three hundred times magnification) capture a wide range of particle size, down to very fine-grained ash (d < 0.1 μm), which cannot be measured reliably using laser diffraction (Riley *et al.*, 2003; Horwell, 2007; Formenti *et al.*, 2011). An unknown amount of bias may arise, however, from using only very small subsamples of particles to measure the particle size distribution.

Table 1. Summary listing the techniques and associated indices used to characterize the physical and mineralogical characteristics of the sample particles. They include laser diffraction (LD), scanning electron microscopy (SEM), gas absorption [helium (H), nitrogen (N_2) and mercury (Hg)], X-ray diffraction (XRD), X-ray fluorescence (XRF) and an electron microprobe (MProbe).

Particle characteristics			Methodology							
			Optical		Gas absorption			Analytical		
Morphology	Type	Definitions	SEM	LD	N_2	He	Hg	XRF	XRD	EMPA
Diameter (m)	Geometric (d_g)	$d_g = \sqrt[3]{LIS}$	✓	✓						
Shape	Sphericity (φ)	$\varphi = (4\pi A)/P^2$								
Density (g cm^{-3})	Bulk (ρ_b)	m/V_b	✓				✓			
	Skeletal (mineral) (ρ_s)	m/V_s	✓			✓			✓	✓
Porosity (%)	Total (ε_t)	$100(1-(\frac{\rho_{Hg}}{\rho_{He}}))$					✓			
	Interparticle (ε_{inter})	$100(V_{inter} - V_{ps})$					✓			
	Intraparticle (ε_{inter})	$100(V_{tp} - V_{inter})/V_b$					✓			
Area (m^2 g^{-1})	Surface area (A_{surf})	See text			✓					
	Cross-section (A_s)		✓							
Hardness		See text							✓	✓
Geochemistry								✓		
Mineralogy									✓	✓

A custom designed algorithm was written using Matlab® image-processing software to analyze the particle image morphology. The image contrast was first adjusted to define clearly the boundary of each particle so that it could be traced (Fig. 3A and C). Particles either intersecting the edges of the camera frame or overlapping other particles were eliminated from the analysis. A total of 2500 discrete (non-aggregated) particle images were analyzed for each of the three volcaniclastic dust samples, providing measurements of the particle perimeter (P; Fig. 3C) and filled area (A). The filled area includes both the closed pores and solid parts of the particle, as bounded by the perimeter of its cross-section. The diameters of the smallest circumscribed and largest inscribed circles were extracted, corresponding to the shortest (S) and longest (L) axes, respectively (Bagheri *et al.*, 2015; Fig. 3C). The intermediate (I) axis is approximated by S because the SEM images are limited to a single projection (two dimensions). The inability to rotate a non-uniform particle to image all sides and angles to obtain multiple projections presents an unknown degree of error associated with the measurement of these dimensions. Other morphological indices were calculated from these fundamental measurements, as for example, the geometric ($d_g = \sqrt[3]{LIS}$) mean diameter (Bagheri *et al.*, 2015). Sphericity ($\varphi = (4\pi A)/P^2$) is an index of the degree to which the shape of a given particle approaches that for a perfect solid sphere, which by definition has a sphericity of one. Increasing particle angularity is represented by progressively smaller values for this index.

In order to examine directly their internal structure and porosity, selected particles with an amorphous, porous surface were milled individually with nanometre-scale precision using a focused ion (gallium) beam (FIB). This process is expensive and time-consuming, with each particle requiring up to 2 h run-time to slice through. High-resolution images then were collected using a LEO 1540 XB field emission-scanning electron microscope (FE-SEM; Zeiss, Oberkochen, Germany) equipped with a secondary electron detector set at an operating voltage of 1.0 kV (Chalmers *et al.*, 2012). The pore size distribution was measured within one milled particle from each of the three Icelandic samples, as required to estimate the particle density (ρ) and porosity (ϵ).

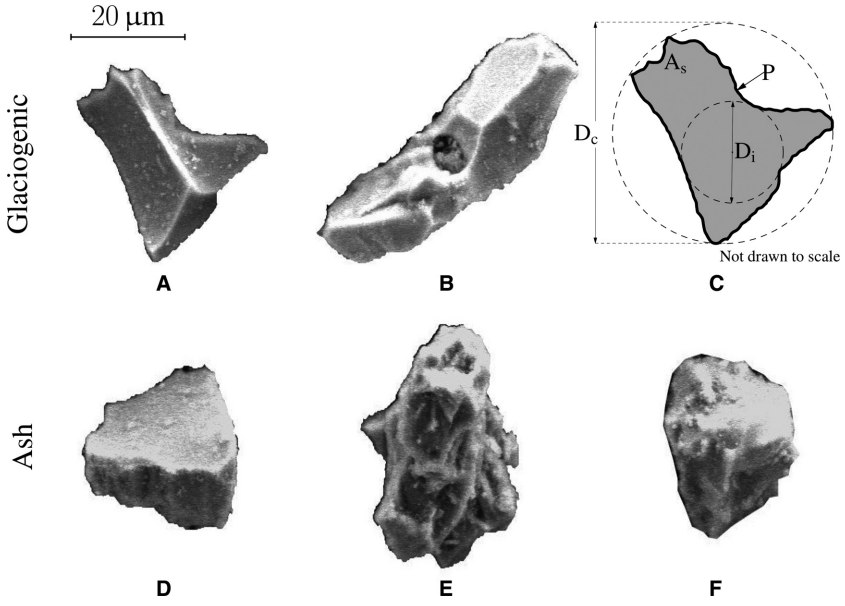

Fig. 3. Representative scanning electron microscopy (SEM) images of selected particles from the glaciogenic – (A) to (C) – and volcanic ash – (D) to (F) – samples. Only particles (A) and (D) are non-vesicular. The schematic (C) of particle (A) defines several geometric attributes along a single projection, inclusive of the filled cross-sectional area, A, and perimeter, P. Also shown are the respective diameters, S and L, of the smallest circumscribed and largest inscribed circles.

Porosity, density and surface area

Helium, nitrogen and mercury intrusion methods were used primarily to measure skeletal density (ρ_s), surface area (A_{surf}) and porosity (ϵ) for each of the three Icelandic samples, respectively (Table 1). Prior to performing each of these measurements, the Icelandic samples were outgassed for 24 h to remove any adsorbed gases, moisture and volatile species. The pores within any given particle can be either open or closed (Fig. 4D) but, together, they constitute the intraparticle pores (Fig. 4). Open pores are

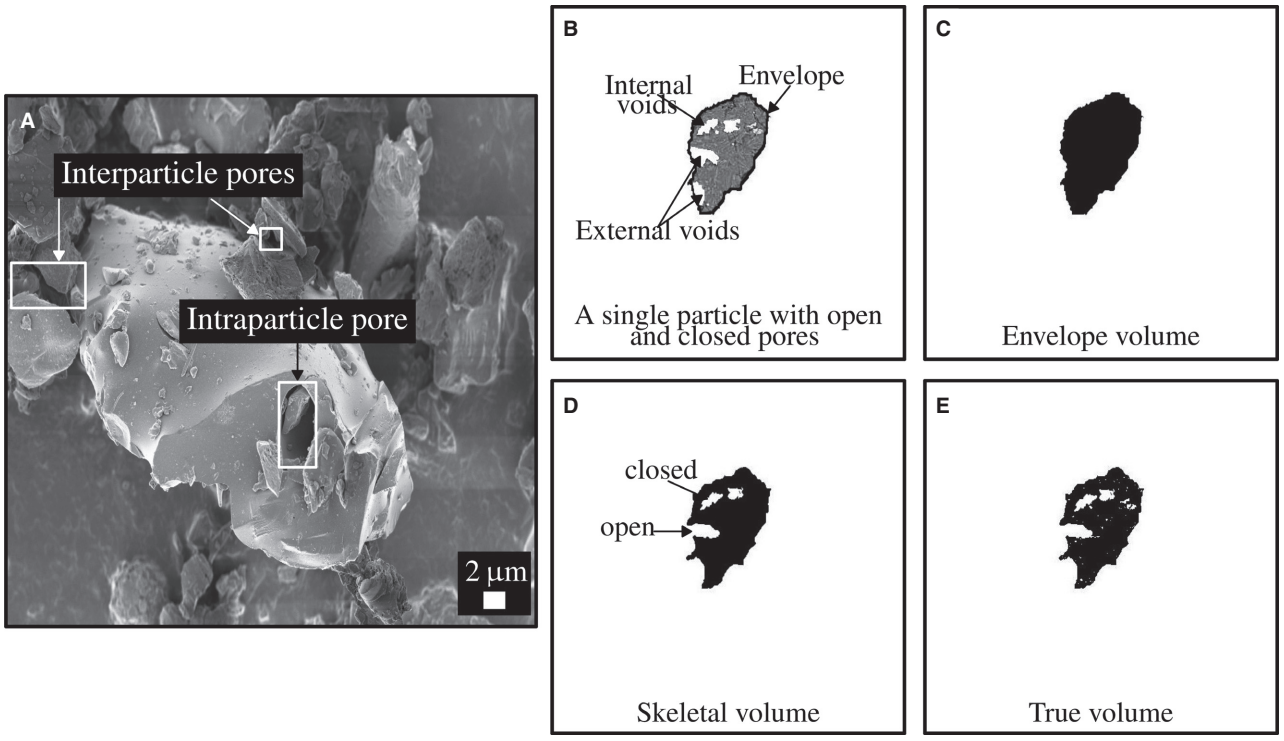

Fig. 4. Distinction between varied pore geometries, as related to the envelope, skeletal and true particle volume.

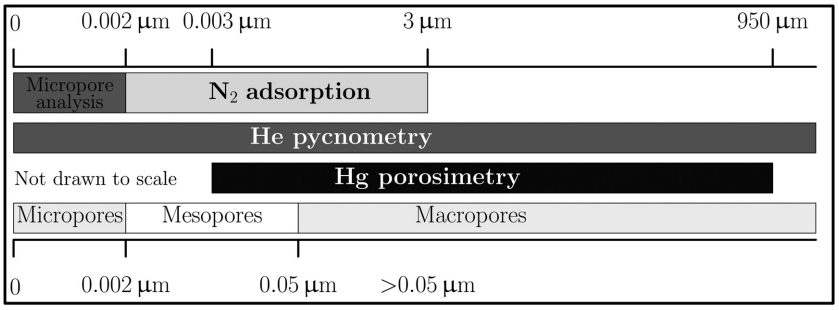

Fig. 5. Pore-size ranges accessible by various analytical techniques used in the present study.

three-dimensional spaces that have connections with the external surface and are formed within and between the particles, whereas closed pores are isolated from the outer surface and may not be accessible by gas absorption. Interparticle pores consist only of the void spaces between particles and are influenced by packing of the bulk sample (Fig. 4A). As summarized in Fig. 5, the intrusion techniques addressed herein vary considerably with regard to the detectable range in pore size.

The skeletal density (ρ_s) of a given sample of particles containing open micropores is best measured using a helium pycnometer. The technique is based on the principle that pressure decreases when a fixed volume of helium is allowed to expand into a confined space, inclusive of intraparticle and interparticle pores (Fig. 4). It can neither be used to measure pore size, nor distinguish between the proportionate amounts of intraparticle versus interparticle pore space. It can only measure the total pore volume of the bulk sample; however, inert helium (He) gas is able to penetrate the smallest pore diameters down to 0.2 nm (Fig. 5) so that the measurement is highly precise. When deducted from the bulk volume of the sample, the true skeletal volume (V_s) is obtained for the solid particles, excluding the net volume of all intruded blind, open intraparticle and interparticle pores detected. Six replicate measurements of the skeletal density for each of the samples were obtained using two separate instruments on the helium gas absorption technique: (i) Micromeritics helium pycnometer (Micromeritics Instrument Corporation, Norcross, GA, USA); and (ii) helium pycnometer. Three replicate measurements of the particle density for the three samples were also obtained using water penetration method.

Matlab image-processing software was also used to measure the pores exposed within the milled particle from each of the three volcanic dust samples, as required to calculate the density. The density ($\rho_s(A_s/A_b)$) was calculated by multiplying the skeletal density (ρ_s) obtained using helium pycnometry by the ratio of the skeletal (solid) area (A_s) to the bulk area (A_b) within the cross-section of the milled particle. The skeletal density calculation omits unexposed and subtle internal pore structures, which may underestimate the total pore volume. The solid area (A_s; Fig. 3C) of the milled particle was calculated from the difference between the bulk area and total pore area ($A_s = A_b - A_p$), where A_p is estimated from the geometric diameter (d_g) of all of the pore spaces identified along the cross-section of the milled particle. A_b is estimated from the geometric diameter of the milled particle cross-section, which is inclusive of all pores and solid. A_p is calculated for either a sphere or an ellipsoid when φ is either >0.7 or <0.7, respectively.

In comparison, mercury porosimetry uses high-pressure intrusion to detect pore diameters ranging from 3 nm to 950 μm (IUPAC, 1994; Quantachrome, 2008, and references within; Fig. 5). The minimal pore diameter limit of 3 nm is within the mesopore range. Liquid mercury cannot intrude micropores unless the applied pressure is sufficient to rupture the pore wall, thereby increasing the pore size to access the pores. Under high pressure, the mercury forced into small pores can cause the bulk sample to compress, especially when the sample contains closed pores, thereby resulting in the detection of too many small to medium pores (Webb & Orr 1997). From this method, the sample porosity (ϵ) can be determined as the percentage ratio of the total pore volume (V_p) to the bulk volume (V_b). Herein, V_p is represented as the total pore volume filled with mercury up to a maximum pressure of 61 000 PSI, and includes the intraparticle (V_{intra}) and interparticle (V_{inter}) pore volumes (Table 1).

The nitrogen adsorption technique is mainly used in material science, but it has recently been applied to volcaniclastic dust analysis with good success (For example, Riley *et al.*, 2003; Alfano *et al.*, 2011; Gislason *et al.*, 2011; Olsson *et al.*, 2013; Urupina *et al.*, 2019). Nitrogen gas adsorption measures either the Brunauer Emmett Teller (specific BET A_{surf}) or total surface area associated with a given sample of particles (Brunauer *et al.*, 1938), inclusive of that for all pore spaces between 2 nm and 3000 nm in diameter (mesopore to macropore) (Fig. 5). Micropores are not detected. The specific BET A_{surf} is based on the measurement of the varied weight of absorbed nitrogen, as determined by its relative pressure, in order to estimate the total exposed surface inclusive of both external and internal void spaces. The total surface area obtained from nitrogen absorption is then divided by the sample mass.

Mineral and phase composition

Small samples (2 g) of fine dust were mounted onto glass slides for X-ray diffraction (XRD) in order to determine their mineralogical composition. The device, a Philips PWR1830 X-ray diffractometer (Philips, Amsterdam, The Netherlands), was operated with copper (Cu) *Kα* radiation (1.5406 Å) at an accelerating voltage of 10 kV and beam current of 10 mA coupled with a nickel (Ni) filter between the X-ray source. For comparison with the helium and mercury intrusion methods, skeletal density was calculated from the sum of the weighted density based on the proportion by weight of the minerals detected and their known (ideal) density. The particle hardness was estimated in a similar way.

The mineral surface phase compositions of the particles were also quantified using a JEOL JXA-8230 electron probe micro-analyzer (EMPA; JEOL Limited, Tokyo, Japan) operated with five wavelength dispersive spectroscopy (WDS). Prior to analysis, samples were first embedded in epoxy moulds to create polished thin sections, following the standard procedure outlined in Hillier & Marshall (1988). A beam diameter of 1 μm with a current of 20 nA and accelerating voltage of 15 kV was used to examine polished sections of the particles without conductive coatings. The phase composition was determined from a combination of analyses, inclusive of phase mapping and SEM imaging of the thin sections. The weight percentage (wt. %) of each phase identified was determined based upon the total exposed surface (cross-sectional area) of each particle in the frame of reference of the microscope. The skeletal density for the samples was calculated from the weight percentages, similar to the XRD results.

Finally, the geochemical composition (showing minor and major elements) of the three Icelandic bulk samples was determined using a PW2404 PANalytical X-ray fluorescence (XRF) spectrometer (Malvern PANalytical, Malvern, UK). Sample preparation required the extraction of aliquots *ca* 6 g of dried particles from each sample, which were then placed in an aluminum cap and compressed to form a pellet.

Table 2. A summary of the major oxides (wt. %) and trace elements (ppm) for the Ash, Glacio1 and Glacio2 samples derived from the PW2404 PANalytical machine.

		Ash	Glacio1	Glacio2
Major oxides (wt.%)	SiO_2	53.33	47.46	47.61
	Al_2O_3	12.80	11.95	11.11
	Fe_2O_3	10.81	14.02	13.57
	CaO	5.18	9.88	6.72
	Na_2O	4.60	2.45	2.58
	MgO	3.11	7.38	4.05
	K_2O	1.88	0.40	1.40
	TiO_2	1.65	1.99	3.20
	P_2O_5	0.45	0.26	0.43
	SO_3	0.22	0.15	0.50
	MnO	0.20	0.20	0.20
Trace elements (ppm)	Chlorine (Cl)	0.08	0.02	0.02
	Barite (Ba)	0.07	nd	0.04
	Zircon (Zr)	0.07	0.02	0.05
	Strontium (Sr)	0.04	0.02	0.04
	Zinc (Zn)	0.02	0.01	0.02
	Yttrium (Y)	0.01	0.004	0.01
	Nickel (Ni)	0.006	0.01	0.01
	Copper (Cu)	0.006	0.02	0.01
	Niobium (Nb)	0.004	nd	0.004
	Rubidium (Rb)	0.003	nd	0.004
	Vanadium (V)	nd	0.03	0.02

nd, not detected.

RESULTS AND DISCUSSION

Geochemistry and mineralogy

The major oxides detected from the XRF analyses (Table 2) are compared in Fig. 6 to those identified for volcaniclastic dust samples collected from similar sites within Iceland. The major oxides Fe_2O_3, Al_2O_3 and SiO_2 in the dust samples have the highest composition and abundance, and showed <10% relevant difference in content

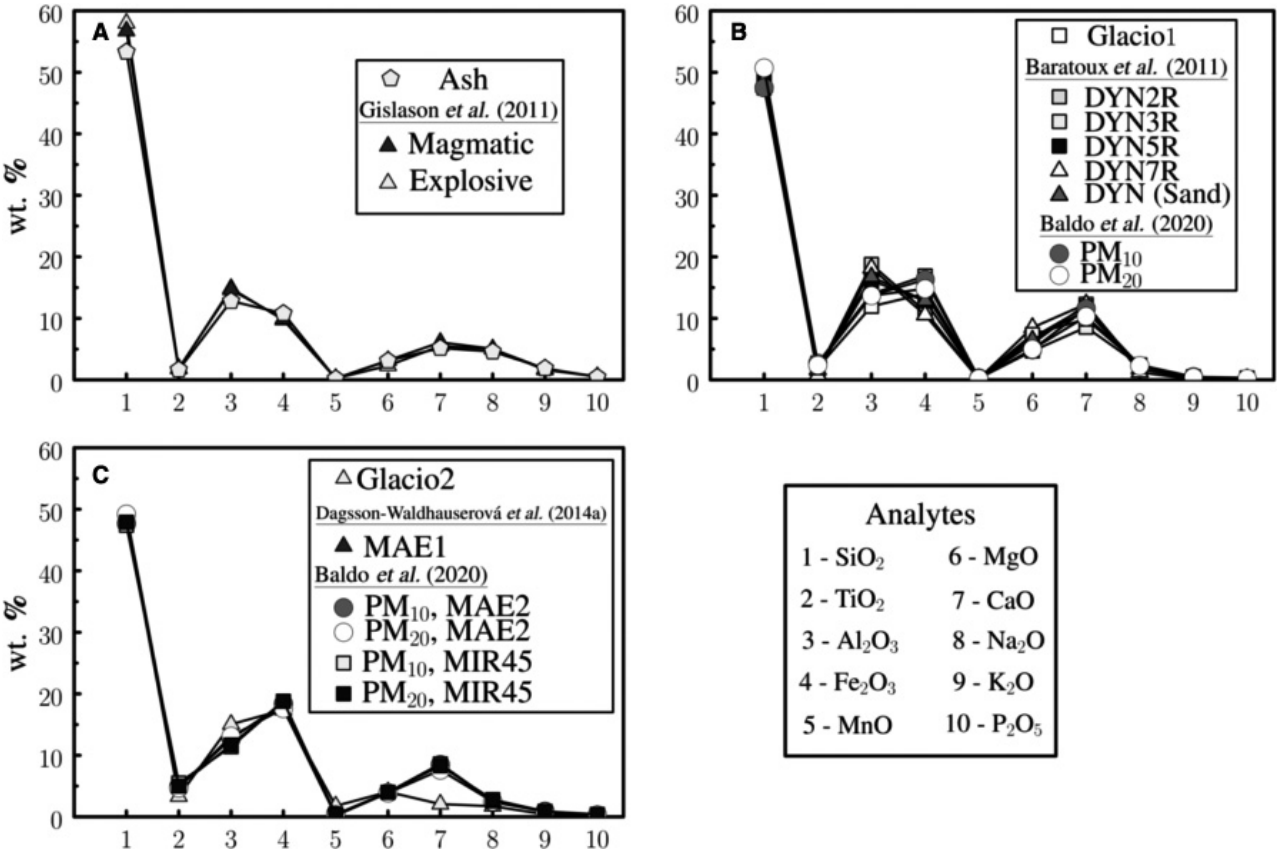

Fig. 6. A comparison of the major oxides identified in this study with published values for samples collected from similar sites. (A) Eyjafjallajökull ash deposits collected on 6 June 2010, weeks after a phase of the explosive eruption that began on 14 April, as compared with samples collected immediately (explosive) and later (typical) during the eruption (Gislason *et al.*, 2011). (B) Dyngjusandur samples from the studies of Baldo *et al.* (2020) and Baratoux *et al.* (2011) versus Glacio1. (C) Markarfljótsaurar (Glacio2), Mælifellssandur (MAE1, MAE2) and Mýrdalssandur (MIR45) samples.

consistent with the study of Baldo *et al.* (2020) for similar sites. The relatively high Fe_2O_3 and Ti_2O_2 compositions indicate that basalts are present in the Icelandic dust samples (Baldo *et al.*, 2020). The 2010 Eyjafjallajökull ash examined in the present study was collected only weeks following the period of eruption and plume generation. The relative abundance of oxides is therefore very similar to values reported by Gislason *et al.* (2011) for explosive and magmatic ash samples collected during the Eyjafjallajökull eruption (Fig. 6A), both early in the event and towards the end, respectively. The SiO_2 content reported for pellets of fine ash isolated in this study by wet sieving is only 5 wt. % less than values reported for bulk ash samples with peak diameter up to 200 μm (magmatic) and 500 μm (typical) in the study of Gislason *et al.* (2011; Fig. 6). The SiO_2 content represents 47 to 53% of the total estimated mass for all samples and is only 1% higher than the range of values obtained for similar sites studied by Baldo *et al.* (2020).

Particle diameter and the location of the collection site within Dyngjusandur appear not to affect the phase composition, given the general similarity evident between the abundance values measured by Baratoux *et al.* (2011) for sand particles, Baldo *et al.* (2020) for PM_{10} and PM_{20}, and those reported herein for dust particles isolated by wet sieving (Fig. 6B). However, the proportion of Al_2O_3 in the dust is marginally lower than for similar samples listed in the studies of Baratoux *et al.* (2011) and Baldo *et al.* (2020). The similarity shown in Fig. 6C between the major oxides detected in dust samples collected from Markarfljótsaurar (Glacio2), Mælifellssandur (MAE1 and MAE2) and Mýrdalssandur (MIR45) is suggestive of similar source materials from Katla and Mýrdalsjökull (Fig. 1B).

The EMPA and XRD results listed in Table 3 also demonstrate good agreement with regard to the mineral compositions identified for both the Eyjafjallajökull ash and glaciofluvial sediments. The Eyjafjallajökull ash is mainly comprised of near equal proportions of plagioclase and amorphous glass (*ca* 40 wt. %), pyroxene (*ca* 10 wt. %), and minor amounts of sanidine and olivine. This composition is consistent with the phase materials reported for Eyjafjallajökull ash in the study of Gislason *et al.* (2011).

In contrast, the glaciofluvial sediments contain a great deal of more glass (for example, Glacio2 up to 70 wt. %) and proportionately less plagioclase (20 to 25 wt. %) consistent with similar sites studied by Baratoux *et al.* (2011) and Baldo *et al.* (2020). Baratoux *et al.* (2011) and Baldo *et al.* (2020) also identify dominant minerals of pyroxene, olivine and plagioclase within thin sections of rock and sand obtained from Dyngjusandur, which is the origin of the Glacio1 collected for this study. The comparatively high proportion of glass (70 to 90 wt. %) reported by Baratoux *et al.* (2011) and Baldo *et al.* (2020) is related to the volcanic activity within glaciers. The large abundance of calcite (11 wt. %; Table 3) detected in Glacio1 appears to be unique to this particular sample.

To summarize, these findings are consistent with earlier work (Baratoux *et al.*, 2011; Gislason *et al.*, 2011; Dagsson-Waldhauserová *et al.*, 2014a; Arnalds *et al.*, 2016; Baldo *et al.*, 2020), which demonstrates that the geochemical and mineralogical compositions of Icelandic dust are dependent on the volcanic dust source. Such connections are useful for the reconstruction of dust transport pathways (Moroni *et al.*, 2018; Đorđević *et al.*, 2019).

Particle size and shape distributions

Laser diffraction (Horiba) measurements of the three wet-sieved Icelandic samples indicate a range in particle diameter between 0.4 μm and 89 μm, with the medians (d_{50}) of the distributions for each sub-sample varying from 12 to 25 μm (Fig. 7). The particle size distribution (PSD) for the Eyjafjallajökull ash is negatively skewed with >80% of the particles lying within the clay-size and silt-size ranges (<20 μm; Fig. 7 A). The distribution for Glacio1 is unimodal (Fig. 7B), whereas that for Glacio2 is bimodal with peaks at 2 μm and 30 μm (Fig. 7C) and a greater proportion of the sample lying within the silt-size range.

Laser diffraction provides an indirect measurement of a given PSD based on a population of particles that is many orders of magnitude larger in number than can be sampled via image analysis. However, the technology is suggested by some workers (Riley *et al.*, 2003; Horwell, 2007; Formenti *et al.*, 2011) to be unreliable for aggregates and irregularly shaped particles ≤10 μm (PM_{10}) that are commonly found in volcanic aerosols and are known to affect human health (Thorsteinsson *et al.*, 2011). The SEM images do allow for direct and highly accurate

Table 3. Summary of the phase classes (wt. %) for the dust particulates from Vík (Ash), Dyngjusandur (Glacio1) and Markarfljótsaurar (Glacio2). A summary of the estimated quantities of phase materials for Mælifellssandur (MAE1) was extracted from the study of Dagsson-Waldhauserová *et al.* (2014a).

METHODS	EMPA			XRD			
Phase	Ash	Glacio1	Glacio2	Ash	Glacio1	Glacio2	MAE1
Volcanic glass	34.2	51.8	74.1	40.0	58.4	71.2	78.2
Plagioclase	45.5	17.0	24.5	36.5	15.8	19.9	12.2
Pyroxene	10.5	17.2	ND	13.7	14.8	0.9	4.6
Sanidine	5.2	ND	0.1	6.4	ND	6.7	ND
Olivine	3.9	0.9	0.1	–	0.1	0.6	1.8
Pyrite	0.7	–	0.3	–	–	–	–
Ilmenite	0.8	1.5	1.0	–	–	–	–
Apatite	0.2	–	–	–	–	–	–
SiO_2	–	–	–	3.3	–	1.1	0.8
Calcite	–	11.7	–	–	11.0	–	–
Zeolite	–	–	–	–	–	–	1.1
Magnetite	–	–	–	–	–	–	0.7

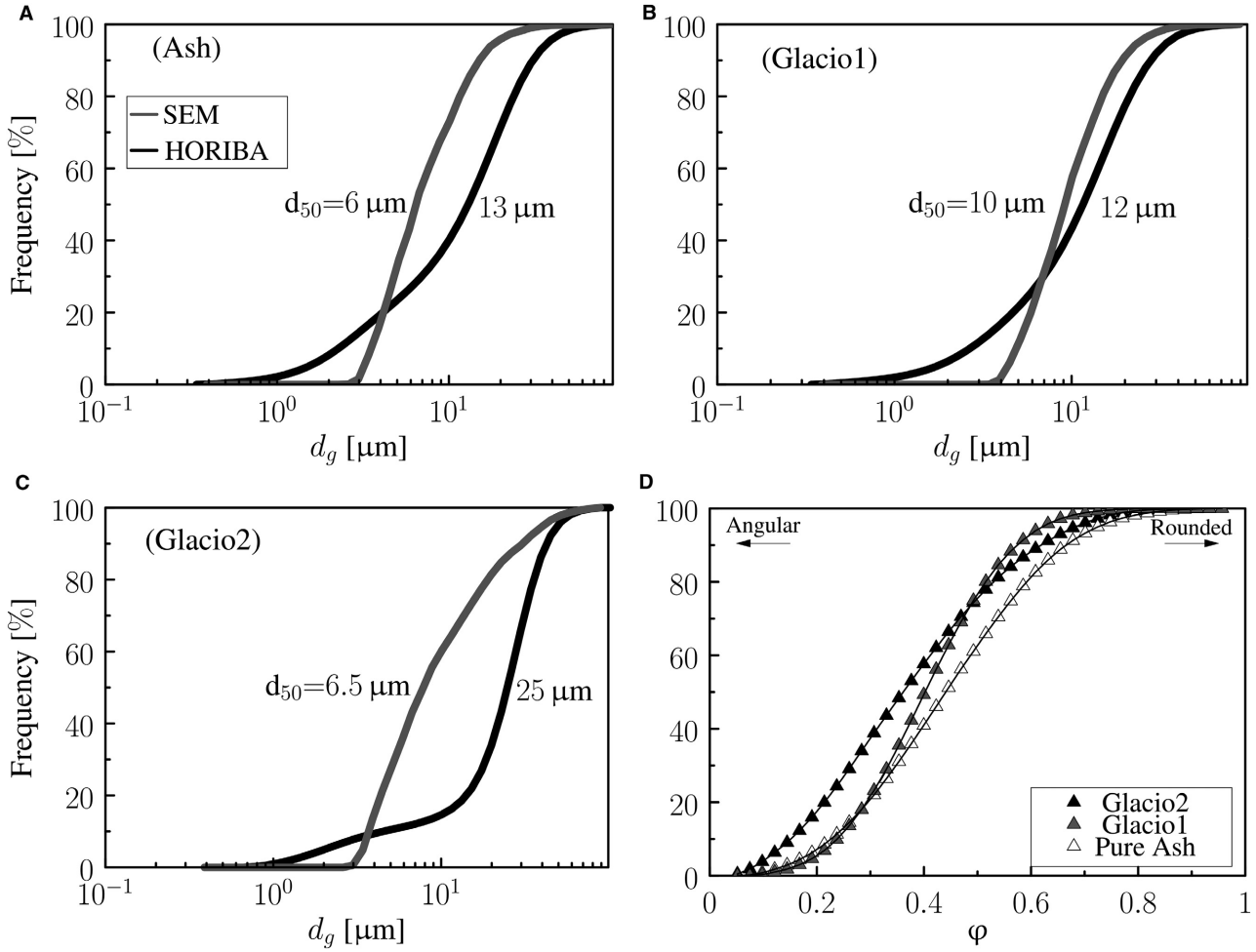

Fig. 7. Cumulative frequency distributions of particle diameter (A) to (C) and sphericity (φ) (D).

measurement of the length and shape characteristics of discrete particles down to nanometre-scale, as identified by the closed boundary of each particle viewed in two dimensions. As a means of comparison, Fig. 7 also provides distributions of the geometric diameter (d_g), based on 2500 random particle images captured for each of the three volcanic dust samples. Notably, the median particle diameters measured via SEM analysis are approximately two to three times smaller than those provided from laser diffraction, while the range also is narrower, suggesting better sorting. Glacio1 demonstrates the best agreement among the measurement approaches, with only a 2 μm difference in the median values. Few particles smaller than 3 to 4 μm in diameter are represented in the SEM data, because these generally appear as 'dust coats' on the surface of larger ones, and they are difficult to identify and isolate.

Figure 7D compares the distributions of particle sphericity (φ), confirming that Icelandic fines have either a non-ideal or highly irregular shape. The modal values for the 2010 Eyjafjallajökull ash, Glacio1 and Glacio2 are given as 0.45, 0.38 and 0.36, respectively. Based on a sample of 300 dust particles (diameter ≤2.5 μm), Butwin *et al.* (2020) report values of φ that range from 0.3 to 0.4, consistent with 2500 measurements obtained in the present study for similar, though coarser (≤65 μm) samples from the 2010 Eyjafjallajökull eruption ($\varphi = 0.45$) and southern Iceland ($0.36 < \varphi < 0.38$). Considerable overlap exists in the tails of the distributions in the present study, particularly between the ash and Glacio1 for $\varphi < 0.3$. Values of φ are binned in Fig. 8 to determine whether or not particle diameter and shape are correlated. Indeed, it would appear that, on average, increasing sphericity is associated with progressively

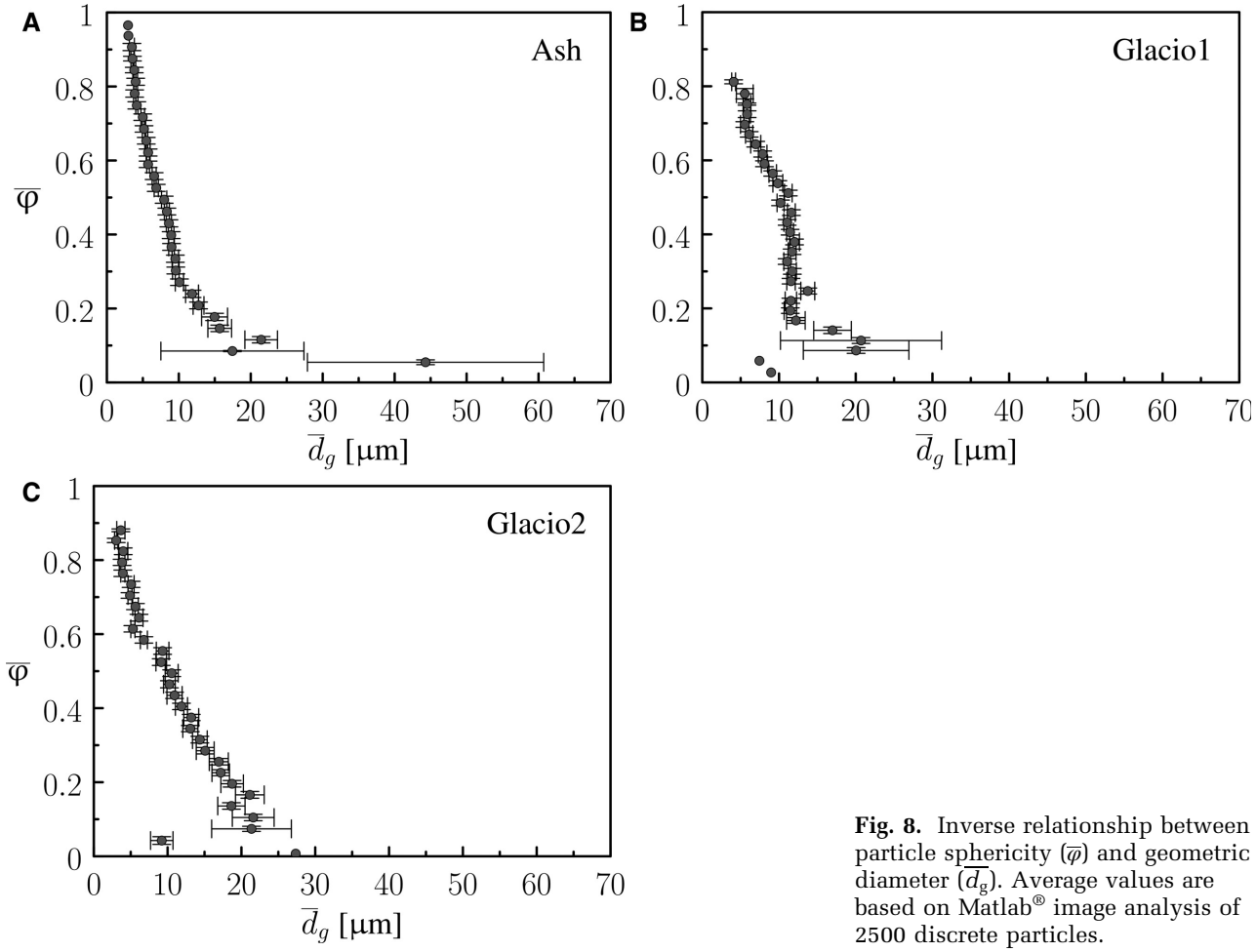

Fig. 8. Inverse relationship between particle sphericity ($\overline{\varphi}$) and geometric diameter ($\overline{d_g}$). Average values are based on Matlab® image analysis of 2500 discrete particles.

smaller particle size, as represented by the mean geometric diameter ($\overline{d_g}$). The results suggest that larger particles up to 65 μm in diameter are more angular and irregular in shape than the fine particles within the sample.

Qualitative observations of morphology from imaging

Additional examples of particle images from each of the Icelandic sources are provided in Fig. 9, at increasing levels of magnification. For the most part, the particle surfaces of the ash and both glaciofluvial sediments can best be described as highly complex, with substantial variation in roughness and porosity that can significantly increase the surface area measured via gas adsorption techniques. The volcanic ash particle (Fig. 9A to C) bears a particularly intricate external structure that appears fragile and could be susceptible to either fracture or chipping (spall) upon impact. In comparison, a sparse coat of nano-scale flakes is apparent on the surface of the particle selected from Glacio1, similar to those identified in SEM images of the volcanic dust used by Butwin *et al.* (2020) and Richards-Thomas and McKenna-Neuman (2020). Relative to the other examples in this figure, this particle appears smooth and crystalline in its general form (Fig. 9D to F). The SEM images of another glaciogenic particle from Glacio2 show that it contains a dense network of distinctive surface pores (Fig. 9G to I). These pores appear to be nested in form and possess particularly delicate sidewalls. Likewise, nano-scale shards of dust are cemented to the walls of the pore sacks within the sand particle image captured for Glacio1 (Fig. 9J to L). Field workers studying dust transport in Iceland speculate that these dust-coats, as well as other frail surface structures, may be fractured and released with repeated inter-particle collisions that occur during active sand transport (saltation) over several kilometres (Mockford *et al.*, 2018; Butwin *et al.*, 2020).

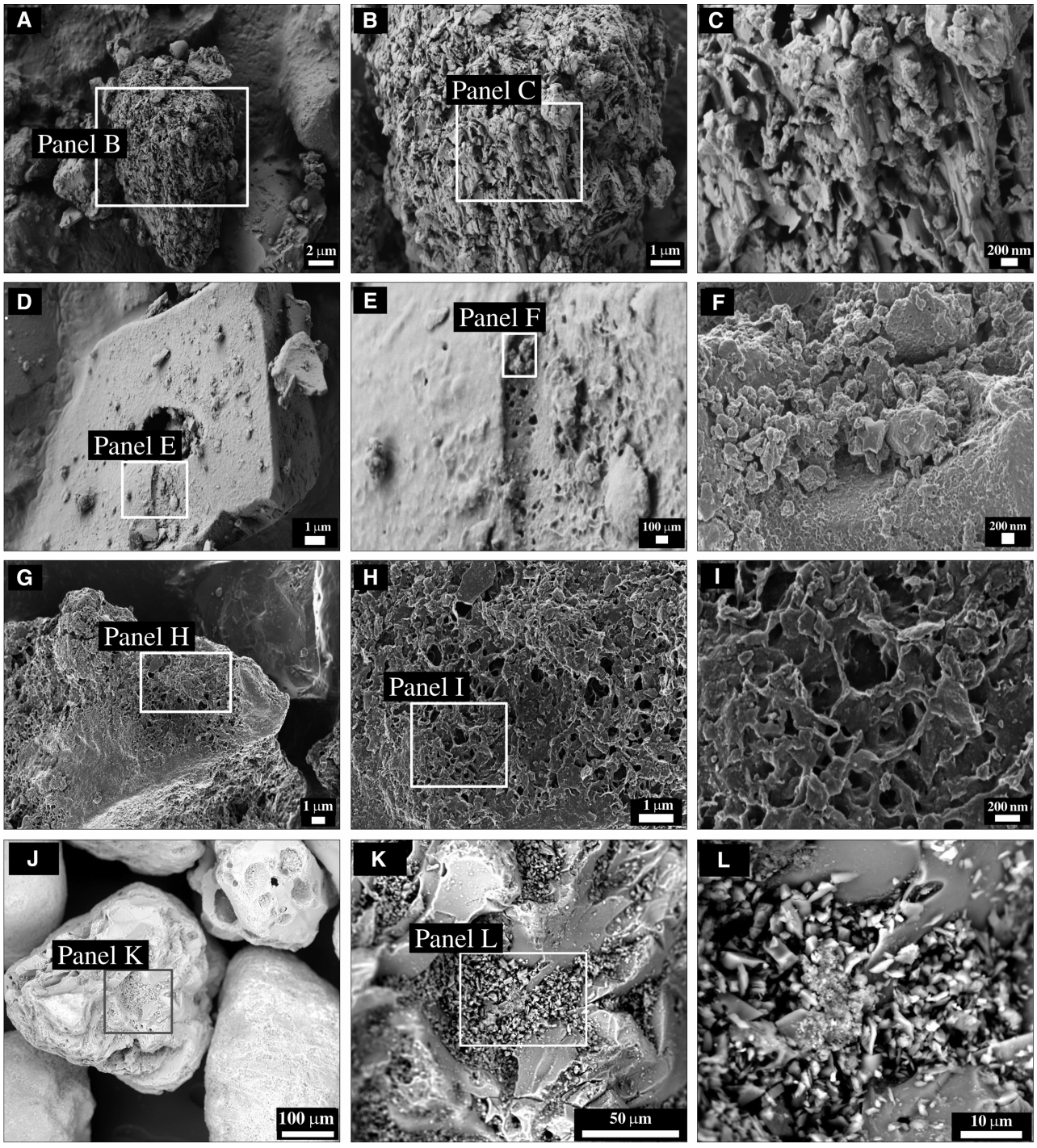

Fig. 9. Scanning electron micrographs of external intrapores on selected particles within the Ash (A) to (C), Glacio1 (D) to (F) and Glacio2 (G) to (I) samples, as well as sand-size glaciogenic particles, that reveal microchips of angular glass-like dustcoats in the sacks of the pores (J) to (L).

Focus ion beam scanning electron microscopic (FIB-SEM) images of a milled volcanic ash particle, 65 μm in diameter, capture the presence of three large internal macropores near the centre of its cross-section, and several fine, irregular-shaped pores (Fig. 10A). Two of

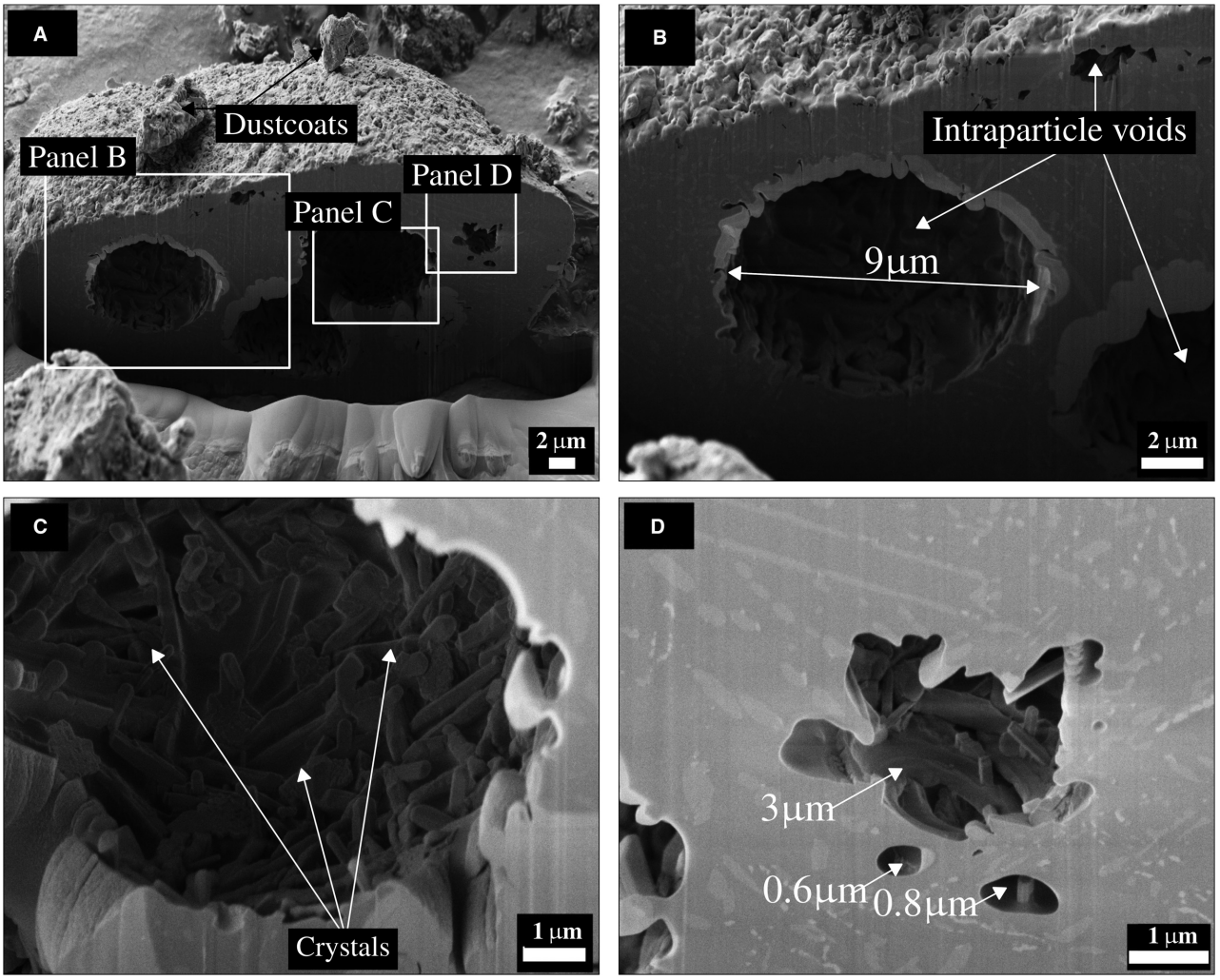

Fig. 10. Scanning electron micrograph of a cross-section created by focused ion beam milling showing the internal structure of a 65 μm Eyjafjallajökull ash particle (A). Macropores identified in each panel are further magnified in subsequent images (B) to (D).

the three large macropores intersect, their diameters ranging from 8 to 10 μm. The macropores are relatively circular, have well-defined edges and contain crystal structure formations (Fig. 10B and C). Fine pores can also be identified near the edge of the milled cross-section with diameters ranging from 0.6 to 1.8 μm (Fig. 10B).

In comparison, the FIB-SEM images of a milled glaciogenic silt particle, 35 μm in diameter, display fine internal macropores, as well as mesopores of irregular shape (Fig. 11). The pore diameters range from 0.02 to 1.25 μm, smaller than those identified for the milled ash particle. The distribution of the internal pore diameters within the cross-section is positively skewed (Fig. 11C), with fine macropores clearly dominating. No micropores appear to be present in the SEM images. Internal pores influence measurements of pore volume and surface area that rely on the adsorption of certain inert gases, because they are less accessible than surface pores, if not completely inaccessible in the case of closed pores. Within a 20 μm particle shown in Fig. 11D, both crystalline and amorphous glass is apparent. The planar facets of the crystalline phase are distinctively smooth and solid, as compared with the fine-scale roughness and high porosity of the amorphous portion. Nano-sized particles, and a 1 to 2 μm fragment of high angularity and distinctively different mineralogy, also adhere to the surface.

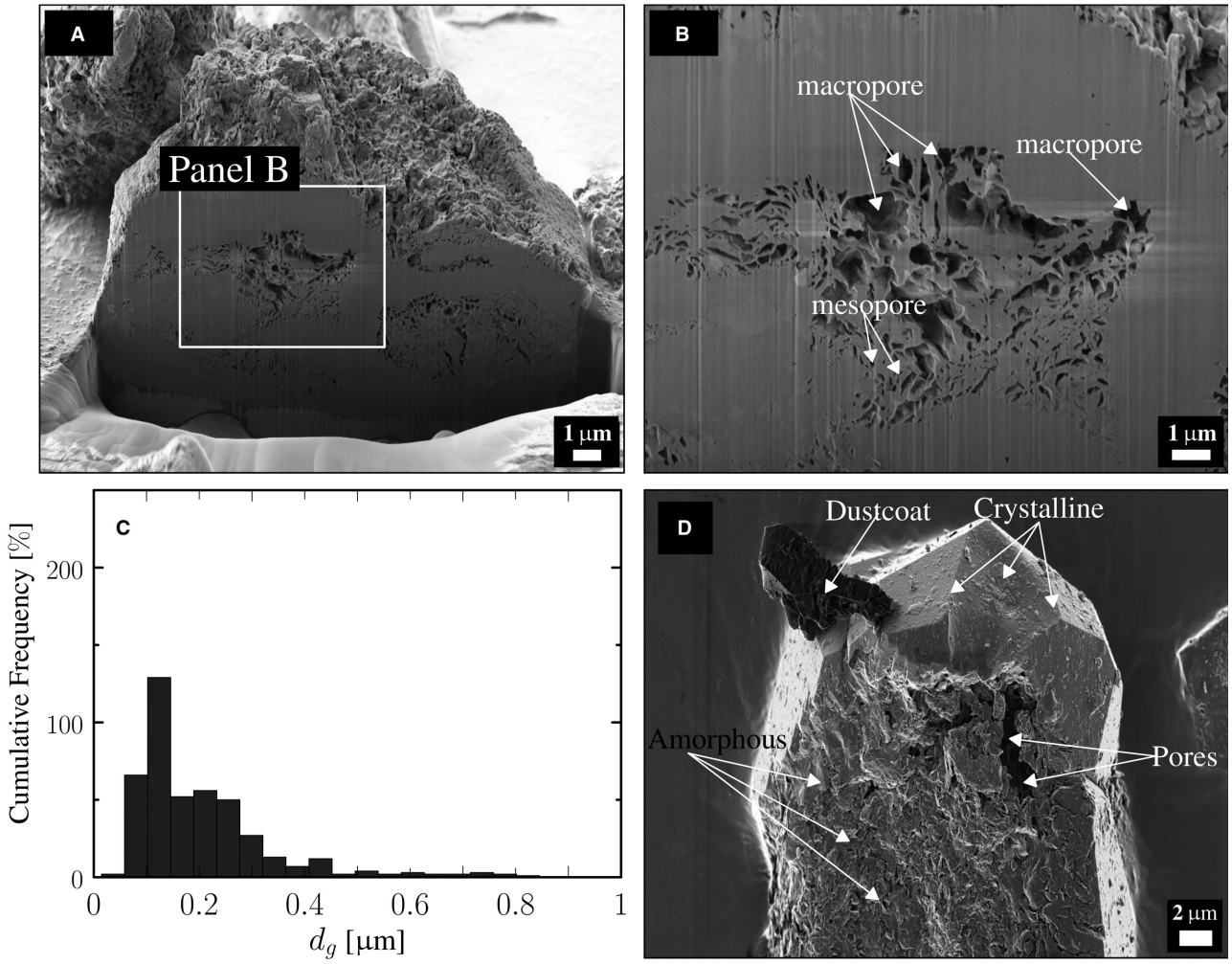

Fig. 11. Focused ion (gallium) beam–scanning electron microscopy (FIB-SEM) images of a 35 μm glaciogenic dust particle with the panel box in (A) magnified in (B) to show details of the mesopores and macropores. The pore-size distribution of the FIB-SEM image of the particle cross-section is shown in (C) while typical features of a glaciogenic particle are shown in (D).

Porosity

The distributions (Fig. 12A) for the interparticle and intraparticle pores, obtained using mercury porosimetry, represent a wide range in pore diameter. Macropores (>0.05 μm) dominate each of the sample distributions, which are slightly negatively skewed. As might be expected, the modal pore diameter estimated from the measured pore volume (Fig. 12) appears to increase as the sample texture coarsens (Fig. 7).

The pore volume measurements allow for the calculation of porosity (Table 1). The interparticle porosity ($\varepsilon_{\text{inter}}$) is the ratio of the interparticle (V_{inter}) and bulk (V_{b}) volumes of the given sample and is governed in part by its packing characteristics. Loose beds yield different interparticle pore volumes than compressed ones, with the latter yielding more reproducible results (Y. León, 1998). The intraparticle porosity ($\varepsilon_{\text{intra}}$) is calculated by dividing the bulk (V_{b}) volume into the difference between the total intruded pore volume (V_{p}) and the interparticle volume (V_{inter}). The total intruded pore volume refers to the total pore volume, within and between the particles that is accessible to mercury.

The pore size distribution of the milled Glacio2 particle shows that the internal pore diameters can be as small as 0.019 μm (Fig. 11C) and suggests that some particles may possess intraparticle and interparticle pore diameters of the same magnitude, making an indirect

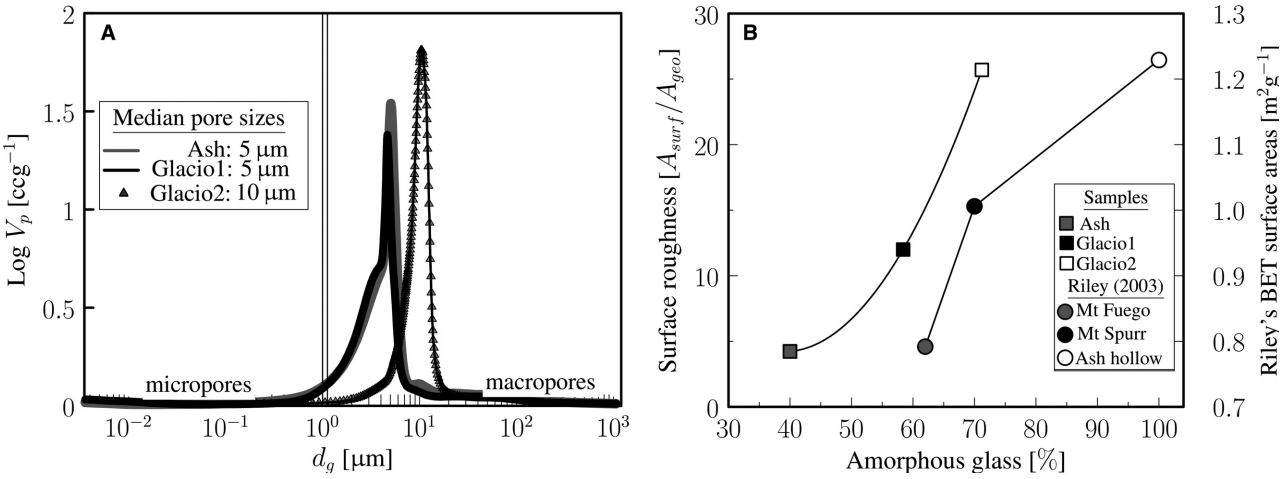

Fig. 12. (A) Pore-size distributions (3 nm to 1 nm). The black vertical solid lines identify the boundaries for the micropores and macropores, with the mesopores lying within the narrow intermediate gap. (B) Relationship between the amorphous glass detected by X-ray diffraction (XRD) analysis (Table 3) and Brunauer Emmett Teller (BET) surface area (A_{surf}, Table 4) for the volcanic dust samples, as compared to ash samples collected in Guatemala (Volcan Fuego), Alaska (Mount Spurr) and Nebraska (Ash Hollow) from the early work of Riley *et al.* (2003).

distinction between them difficult. Therefore, there is no distinction between the range of sizes for the interparticle and intraparticle pores of the three volcaniclastic dust samples used to conduct this study. The distributions of intraparticle and interparticle pores range from 2 to 3000 nm in size within the three volcanic dust samples (Fig. 12A).

The pore size distributions for the ash and Glacio1 appear to overlap, while their Horiba particle size distributions are also similar (Fig. 7A and B). Consistent with this association, Glacio2 contains both larger particles and voids (Fig. 7C). Butwin *et al.* (2020) suggest that relatively large, angular shaped (Fig. 8) particles with low density (Table 4) and high porosity (Fig. 12A) are indeed entrained, suspended and transported over long distances in the atmosphere, presumably because of their low mass.

Surface area

Table 4 summarizes the specific surface area data obtained from the BET measurements. At 1.65 m^2 g^{-1}, A_{surf} for the 2010 Eyjafjallajökull ash is lower than, by more than a factor of two, the values obtained for either Glacio1 (4.19 m^2 g^{-1}) or Glacio2 (5.14 m^2 g^{-1}). Explosive and magmatic ash (Fig. 6) are reported in the literature to have specific BET surface areas of 4.3 m^2 g^{-1} (Gislason *et al.*, 2011; Olsson *et al.*, 2013) and 0.45 m^2 g^{-1} (Gislason *et al.*, 2011), respectively, bracketing the values obtained for ash in the present study. The specific BET A_{surf} of 1.65 m^2 g^{-1} for the ash is similar to the volcaniclastic dust collected from Mýrdalssandur (1.5 m^2 g^{-1}; Urupina *et al.*, 2019), but higher than magmatic ash (0.75 m^2 g^{-1}) sampled by the same authors for the Eyjafjallajökull eruption in 2010. The surface area measurements for Glacio2 were replicated using two separate instruments based on the nitrogen gas adsorption technique: the Poremaster and Gemini VII 2390 (Micromeritics). The results obtained are relatively similar, differing by only 0.07 m^2 g^{-1}. As expected, A_{surf} values obtained from mercury porosimetry (6.34 to 14.36 m^2 g^{-1}) are three to four times higher than the corresponding BET measurements (Table 4), suggesting that mercury can penetrate large pore diameters up to 900 μm. The upper limit for pore detection is 3 μm when using the nitrogen gas absorption technique (Fig. 5). Mercury porosimetry is also affected by variation in particle alignment and pore wall collapse under high pressure. Values reported by Urupina *et al.* (2019) for the specific BET A_{surf} (7 ± 1.8 m^2 g^{-1}) of similar samples obtained from Dyngjusandur fall between those obtained in the present study (for example, 4 m^2 g^{-1} via BET and 12 m^2 g^{-1} via mercury porosimetry).

The geometric diameter (d_g) determined for each of the samples was used to calculate the

Table 4. A summary of the measured and calculated particle characteristics (Table 1), inclusive of surface area, density (bulk and skeletal), porosity and hardness

Parameters		Analytical techniques	Sample portions and assumptions	Icelandic dust samples		
				Ash	Glacio1	Glacio2
Surface area (m^{-2} g^{-1})	Measured	BET nitrogen absorption	(1 to 2 g)	1.65	4.20	5.14
		Mercury intrusion		6.34	11.58	14.36
	Calculated	Horiba particle sizing	(1 to 2 g) Spherical assumption	0.33	0.32	0.10
		Horiba (geometric)		0.39	0.35	0.20
		SEM image analysis	(2500 particles)			
			Cylinder	0.34	0.23	0.33
			Cube	0.62	0.39	0.59
			Ellipsoid	0.26	0.17	0.26
			Disc	0.10	0.07	0.09
			Sphere	0.41	0.26	0.20
Density (g cm^{-3})	Measured	Mercury	(1 to 2 g)	1.17*	1.26*	1.12*
		Mercury		1.77***	1.75***	2.32***
		Helium$^{(1)}$		2.66**	2.79**	2.74**
		Helium$^{(2)}$		2.72**	2.86**	2.77**
		Water	(10 to 11 g)	2.72***	2.65***	2.26***
	Calculated	XRD	(1 to 2 g)	2.63**	2.59**	2.45**
		EMPA	Embedded particles	2.68**	2.67**	2.46**
		SEM image analysis	Milled particle	1.73** ($\rho^{(1)}\downarrow$35%)	2.46** ($\rho^{(1)}\downarrow$12%)	2.02** ($\rho^{(1)}\downarrow$26%)
Pore volume (cm^3)	Measured	Mercury intrusion	(2 g)			
			Intraparticle	0.078	0.082	0.022
			Interparticle	0.09	0.068	0.15
			Total	0.167	0.149	0.172
Porosity (%)			Intraparticle	29.44	33.65	7.41
			Interparticle	33.97	27.88	51.81
			Total	63.41	61.53	59.23
Moh's hardness	Calculated	XRD	(6 g)	5.80	5.19	5.50
		EMPA	Embedded particles	5.53	5.23	5.50

*ρ_b - Bulk density. **ρ_s - Skeletal density. ***ρ_p - Particle density.

corresponding surface area for several idealized particle shapes (cylinders, cubes, ellipsoids, discs and spheres). All calculated values were found to be substantially smaller than the BET measurements, by as much as three orders of magnitude (Table 4). This result clearly shows that image analysis along a single two-dimension projection does not adequately capture the

complex surface structures that determine A_{surf}. Similar to the earlier work of Riley *et al.* (2003), calculations of the specific surface area of particles assumed to be spherical in shape, based on particle diameter measurements obtained by laser diffraction for each Icelandic sample, also grossly underestimate values of BET A_{surf} obtained by nitrogen adsorption. The study of Riley *et al.* (2003) was conducted on volcanic ash collected in Guatemala (Volcan Fuego), Alaska (Mount Spurr) and Nebraska (Ash hollow member). In this case, surface areas estimated for the ash ($0.33\ m^2\ g^{-1}$) and Glacio1 ($0.32\ m^2\ g^{-1}$) are nearly triple those for Glacio2 ($0.1\ m^2\ g^{-1}$) as listed in Table 4, which again fails to represent the correct ranking identified by direct measurement consistent with the findings of Riley *et al.* (2003).

Figure 12 suggests that the specific BET A_{surf} scales positively with the abundance of amorphous glass, in the case of both the Icelandic volcanic dust samples and the varied sources of ash studied by Riley *et al.* (2003). However, in the latter case, the median diameter was somewhat coarser (25 to 77 μm) and the particles less porous (Fig. 12B). Indeed, Fig. 11D shows a particle that has both crystalline and amorphous areas with the latter being irregularly shaped, rough and porous, thereby providing a greater surface area compared to the smooth solid faces of the crystalline portion. Amorphous glass is most likely to form at early stages, during the cooling process. Volcanic dust containing amorphous glass can be angular, sharp and porous with large specific surface area allowing particles up to 50 μm in diameter to be transported over long distances (Navratil *et al.*, 2013).

Density

As compared to Eyjafjallajökull Ash, the true skeletal density (ρ_s) of most glaciogenic sediments in Iceland is not well-documented. Although the measured surface areas were found to be substantially different, the density measured using helium pycnometry (Table 4) is similar for the three Icelandic samples: Ash (lowest at 2.66 to 2.72 g cm^{-3}), Glacio1 (2.79 to 2.86 g cm^{-3}) and Glacio2 (2.74 to 2.77 g cm^{-3}), but greater than that of rhyolite glass (2.3 g cm^{-3}). In comparison, the particle densities calculated from the proportional weight of solid minerals detected within the samples (i.e. using XRD phase and EMPA composition) are slightly lower: Ash (2.63 to 2.68 g cm^{-3}), Glacio1 (2.59 to 2.67 g cm^{-3}) and Glacio2 (2.45 to 2.46 g cm^{-3}), with the Ash having the highest density (Table 4).

The densities calculated from SEM images of the milled Ash, Glacio1, and Glacio2 particles (shown in cross-section in Figs 10 and 11) are 1.73 g cm^{-3}, 2.46 g cm^{-3} and 2.02 g cm^{-3}, respectively. Skeletal density measurement, based on the analysis of an SEM image of a given particle cross-section, excludes the volume of the internal and surface pores observed. However, the sample size is usually unacceptably small. The estimated skeletal densities of the milled particle cross-sections are about 35%, 12% and 26% less than that of the measured skeletal density of the Ash, Glacio1 and Glacio2 samples, respectively (Table 4). If the intraparticle pores are inaccessible, although sufficiently large to decrease the particle density by up to 35%, then the true skeletal density (ρ_s) could be overestimated by measurements from a helium pycnometer. The bulk densities were all found to be extraordinarily low, *ca* 1.1 to 1.3 g cm^{-3} but near identical in magnitude (Table 4).

The particle densities measured using the water penetration method are 2.72 g cm^{-3}, 2.65 g cm^{-3} and 2.26 g cm^{-3} for the Ash, Glacio1 and Glacio2, respectively (Table 4), as referenced against those measured for four well-known minerals (for example, Silica sand, Olivine, Wollastonite and Brucite). The particle densities obtained using water pycnometry are well within the range reported in the published literature (Kretz, 1980), although the minerals used were not pure. However, calculations of the particle density based on measurement of particle mass and volume obtained via mercury porosimetry, differ substantially from and are often lower than (Ash, 1.77 g cm^{-3}; Glacio1, 1.75 g cm^{-3} and Glacio2, 2.32 g cm^{-3}) those for the water penetration method (Table 4). A comparative measurement obtained for Icelandic ash (2.25 g cm^{-3}) by Butwin *et al.* (2020), again using a water pycnometer, falls directly between the two values for Eyjafjallajökull ash reported in Table 4 for this study.

Dynamical effects of the particle geometry

In theory, the micro-scale particle properties described above (for example, angular morphology, high porosity and nano-scale dustcoats shown in Figs 9 and 10) may influence rates of dust entrainment, emission and deposition in

Iceland. The magnitude of this influence is unaccounted for in dust models wherein an idealized geometric form, for example, a solid sphere, often is used to approximate natural particles.

A particle falling through a column of air reaches terminal velocity when its weight (F_g) is balanced by the opposing fluid drag (F_d), assuming that all other forces acting on the particle are negligible. F_g is determined by the product of the particle mass (m) and gravitational acceleration (g), where m is approximated by the product of its density (ρ) and volume (V), inclusive of its intraparticle pores (V_{intra}) and skeletal volume (V_s). F_d can be approximated from the quadratic stress law:

$$F_d = \frac{1}{2}\rho_a w^2 A_p C_d \quad (1)$$

requiring values for the air density (ρ_a), relative particle velocity (w), projected area of the particle (A_p) and drag coefficient (C_d). As a coarse approximation, the settling rate of a given particle can be taken to scale with $\sqrt{\rho V/A_p}$, which for an idealized sphere reduces to $\sqrt{\rho d_g}$.

In illustration of such effects, three particle images (Fig. 13) were selected for analysis, all having an identical geometric diameter (10 μm or PM_{10}), but varying shape, density and origin. A_p was measured to be 85.7 μm^2 for the solid glass sphere, with only a 3% variation from the value calculated for a perfect solid sphere. The cross-sectional areas measured for the ash and glaciogenic particles were up to 30% larger at 111.6 μm^2 and 111.7 μm^2, respectively. As expected, particle densities measured for the porous Icelandic particles (for example, 1.8 g cm^{-3}, 1.7 g cm^{-3} and 2.3 g cm^{-3} for the Ash, Glacio1 and Glacio2 particles, respectively), based on V obtained from mercury porosimetry, all fall below that for the solid glass sphere (2.5 g cm^{-3}). Notably, the density for particles from Glacio2 is similar to that of rhyolite glass. Examination of the milled particles (Figs 10 and 11) would suggest that, if the inaccessible internal pores are accounted for, the density could be as much as 25% lower. A comparison between calculations of $\sqrt{\rho V/A_p}$ would therefore suggest that:

1 the settling velocity of Icelandic dust in still air may be as little as 20% of that for a solid glass sphere of equivalent (geometric mean) diameter, and from this

2 the estimated residence time of volcaniclastic dust in still air may be longer (by a factor of

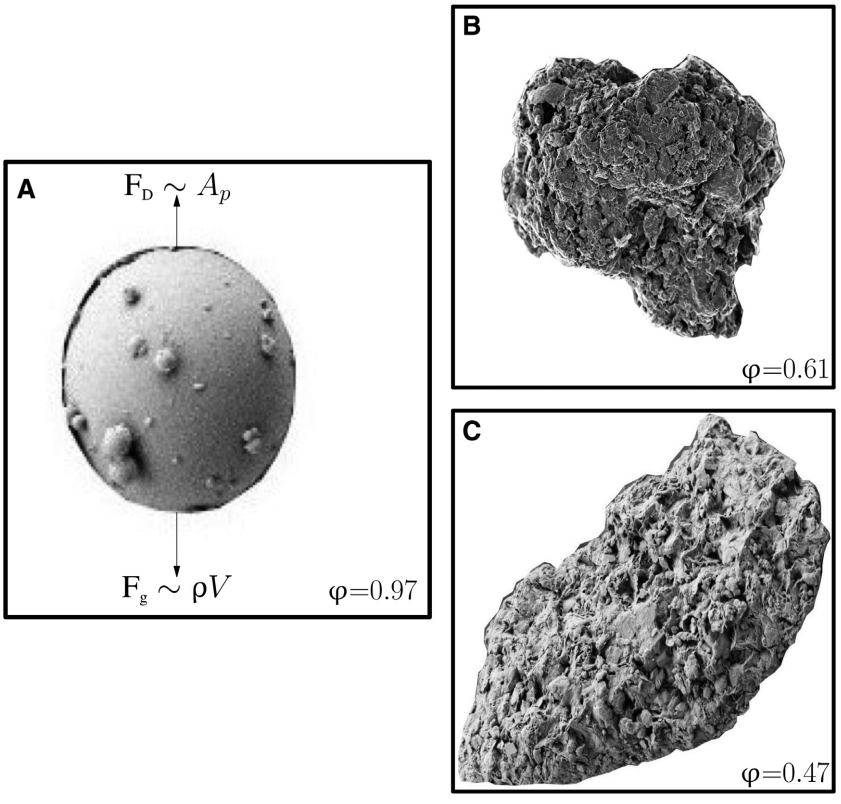

Fig. 13. Selected PM_{10} particles with varied shape, density and origin, as used to estimate the influence of geometry on the particle settling rate.

five) than calculated for idealized spherical particles.

These approximations should be revisited in controlled laboratory experiments where both particle–fluid and particle–particle interactions come into play. One further factor not accounted for in this dynamical analysis concerns the effects of particle shape and roughness on the drag coefficient (C_d), where a change in the value of this parameter may either offset or enhance the influence of the enlarged silhouette area. Finally, the diminishing particle porosity (increasing density) observed with reduced diameter would suggest that the deposition rate of an idealized solid form of equivalent size may be a reasonable approximation of that for the finest aerosols of volcanic origin.

CONCLUSIONS

Dust (PM_{10}) sources within Iceland include basaltic glaciogenic sediments and volcanic ash. The particles derived from these sites are characterized by unique physical properties that may affect rates of entrainment and deposition within the atmospheric boundary layer. They have a high degree of porosity that is shown in this study to increase with the proportion of amorphous glass. This reduces their apparent density, and therefore their weight, relative to a solid mineral particle of equivalent volume. In a turbulent boundary layer, this lower weight is expected to reduce the amount of lift required to maintain such particles in suspension and potentially increase their residence time in still air by a factor of five.

The low sphericity, rough surface texture and high porosity of the Icelandic particles investigated in this study are shown to produce very large surface areas, as measured via gas adsorption. The implications for dust transport are two-fold:

- Abundant numbers of shard-like, nano-scale 'fragments' are observed in SEM images to adhere to the particle surfaces as 'flaky dust coats', while the highest concentrations appear within meso-scale to macro-scale pores. Some fraction of these dust coatings could be released as aerosols into the atmospheric boundary layer through the abrasion that occurs with sand drifting during wind erosion events.
- Water adsorption onto these capacious particle surfaces, and absorption within the pore spaces, may be sufficient to influence the rate of particle deposition through the growth of water films and lenses, as well as particle interactions that lead to aggregation, thereby affecting cloud condensation, precipitation and the radiation balance.

Laboratory experiments, in which particle settling is measured with high accuracy under the cool humid conditions characteristic of Iceland's climate, are further needed to evaluate and quantify these proposed effects.

ACKNOWLEDGEMENTS

The authors wish to thank Throstur Thorsteinsson (University of Iceland) and Pavla Dagsson-Waldhauserova (The Agricultural University of Iceland), as well as Tom Mockford (University of Loughborough), for providing the field samples examined in this study. George Kretschmann, Mike Gorton, and Yanan Liu from the Earth Sciences Centre at the University of Toronto provided valuable insight into the mineral and phase compositions, using an X-ray diffractometer and JEOL JXA8230 5-WDS electron microprobe, respectively. Sterling Vanderzee from the Department of Earth, Ocean and Atmospheric Sciences at the University of British Columbia provided skeletal density measurements using Helium gas. This study was supported by the Natural Sciences and Engineering Research Council of Canada (NSERC) and the Canada Foundation for Innovation (CFI) through separate grants awarded to C. McKenna-Neuman and I. Power. The authors sincerely wish to thank the Reviewers and the Associate and Chief Editors for their efforts in reading through the manuscript and giving critical feedback that was insightful and beneficial to improve the article.

DATA AVAILABILITY STATEMENT

The particle characteristics datasets that support the findings of this study are openly available from Trent University Library Research Data Repository: Scholars Portal Dataverse, V1 at https://doi.org/10.5683/SP2/ASQ5GC.

REFERENCES

Alfano, F., **Bonadonna, C.**, **Volentik, A.C.M.**, **Connor, C.B.**, **Watt, S.F.L.**, **Pyle, D.M.** & **Connor, L.J.** (2011) Tephra

stratigraphy and eruptive volume of the May, 2008, Chaitén eruption, Chile. *Bull. Volcanol.*, **73**, 613–630.

Arnalds, Ó. (2010) Dust sources and deposition of aeolian materials in Iceland. *Iceland. Agri. Sci.*, **23**, 3–21.

Arnalds, Ó., **Dagsson-Waldhauserová, P.** and **Olafsson, H.** (2016) The Icelandic volcanic aeolian environment: Processes and impacts – a review. *Aeol. Res.*, **20**, 176–195.

Arnalds, Ó., **Ólafsson, H.** and **Dagsson-Waldhauserová, P.** (2014) Quantification of iron-rich volcanogenic dust emissions and deposition over the ocean from Icelandic dust sources. *Biogeosciences*, **11**, 6623–6632.

Arnalds, Ó., **Thorarinsdottir, E.F.**, **Thorsson, J.**, **Waldhauserová, P.D.** and **Agustsdottir, A.M.** (2013) An extreme wind erosion event of the fresh Eyjafjallajökull 2010 volcanic ash. *Scient. Rep.*, **3**, 1–7.

Arnalds, Ó., **Gisladottir, F.O.** and **Sigurjonsson, H.** (2001a) Sandy deserts of Iceland: an overview. *J. Arid Environ.*, **47**, 359–371.

Arnalds, Ó., **Thorarinsdoittir, E.F.**, **Metusalemsson, S.**, **Jonsson, A.**, **Gretarsson, E.** and **Arnason, A.** (2001b) Soil Erosion in Iceland. Gutenberg. https://doi.org/isbn9979-60-641-X.

Bagheri, G.H., **Bonadonna, C.**, **Manzella, I.** and **Vonlanthen, P.** (2015) On the characterization of size and shape of irregular particles. *Powder Technol.*, **270**(A), 141–153.

Baldo, C., **Formenti, P.**, **Nowak, S.**, **Chevaillier, S.**, **Cazaunau, M.**, **Pangui, E.**, **Di Biagio, C.**, **Doussin, J.F.**, **Ignatyev, K.**, **Dagsson-Waldhauserová, P.** and **Arnalds, O.** (2020) Distinct chemical and mineralogical composition of Icelandic dust compared to North African and Asian dust. *Atmos. Chem. Phys. Disc.*, **20**, 13521–13539.

Baratoux, D., **Mangold, N.**, **Arnalds, Ó.**, **Bardintzeff, J.M.**, **Platevoët, B.**, **Grégorie, M.** and **Pinet, P.** (2011) Volcanic sands of Iceland-diverse origins of aeolian sand deposits revealed at Dyngjusandur and Lambahraun. *Earth Surf. Proc. Land.*, **36**, 1789–1808.

Boy, M., **Thomson, E.S.**, **Acosta Navarro, J.-C.**, **Arnalds, Ó.**, **Batchvarova, E.**, **Bäck, J.**, **Berninger, F.**, **Bilde, M.**, **Brasseur, Z.**, **Dagsson-Waldhauserova, P.**, **Castarède, D.**, **Dalirian, M.**, **de Leeuw, G.**, **Dragosics, M.**, **Duplissy, E.-M.**, **Duplissy, J.**, **Ekman, A.M.L.**, **Fang, K.**, **Gallet, J.-C.**, **Glasius, M.**, **Gryning, S.-E.**, **Grythe, H.**, **Hansson, H.-C.**, **Hansson, M.**, **Isaksson, E.**, **Iversen, T.**, **Jonsdottir, I.**, **Kasurinen, V.**, **Kirkevåg, A.**, **Korhola, A.**, **Krejci, R.**, **Kristjansson, J.E.**, **Lappalainen, H.K.**, **Lauri, A.**, **Leppäranta, M.**, **Lihavainen, H.**, **Makkonen, R.**, **Massling, A.**, **Meinander, O.**, **Nilsson, E.D.**, **Olafsson, H.**, **Pettersson, J.B.C.**, **Prisle, N.L.**, **Riipinen, I.**, **Roldin, P.**, **Ruppel, M.**, **Salter, M.**, **Sand, M.**, **Seland, Ø.**, **Seppä, H.**, **Skov, H.**, **Soares, J.**, **Stohl, A.**, **Ström, J.**, **Svensson, J.**, **Swietlicki, E.**, **Tabakova, K.**, **Thorsteinsson, T.**, **Virkkula, A.**, **Weyhenmeyer, G.A.**, **Wu, Y.**, **Zieger, P.** and **Kulmala, M.** (2019) Interactions between the atmosphere, cryosphere, and ecosystems at northern high latitudes. *Atmos. Chem. Phys.*, **19**, 2015–2061.

Brunauer, S., **Emmett, P.H.** and **Teller, E.** (1938) Adsorption of gases in multimolecular layers. *J. Am. Chem. Soc.*, **60**, 309–319.

Butwin, M.K., **von Löwis, S.**, **Pfeffer, M.A.** and **Thorsteinsson, T.** (2019) The effects of volcanic eruptions on the frequency of particulate matter suspension events in Iceland. *J. Aer. Sci.*, **128**, 99–113.

Butwin, M.K., **Pfeffer, M.A.**, **von Löwis, S.**, **Støren, E.W.N.** and **Thorsteinsson, T.** (2020) Properties of dust source material and volcanic ash in Iceland. *Sedimentology*, **67**, 3067–3087.

Bullard, J., **Baddock, M.**, **Bradwell, T.**, **Crusius, J.**, **Darlington, E.**, **Gaiero, D.**, **Gassó, S.**, **Gisladottir, G.**, **Hodgkins, R.**, **McCulloch, R.** and **McKenna-Neuman, C.** (2016) High-latitude dust in the earth system. *Rev. Geophys*, **54**(2), 447–485.

Cannone, N., **Diolaiuti, G.**, **Guglielmin, M.** and **Smiraglia, C.** (2008) Accelerating climate change impacts on alpine glacier forefield ecosystems in the European Alps. *Ecol. Appl.*, **18**, 637–648.

Carlsen, H.K., **Gislason, T.**, **Forsberg, B.**, **Meister, K.**, **Thorsteinsson, T.**, **Jóhannsson, T.**, **Finnbjornsdottir, R.** and **Oudin, A.** (2015) Emergency hospital visits in association with volcanic ash, dust storms and other sources of ambient particles: a time-series study in Reykjavík, Iceland. *Int. J. Env. Res. Pub. Health*, **12**, 4047–4059.

Chalmers, G.R., **Bustin, R.M.** and **Power, I.** (2012) Characterization of gas shale pore systems by porosimetry, pycnometry, surface area, and field emission scanning electron microscopy/transmission electron microscopy image analyses: examples from the Barnett, Woodford, Haynesville, Marcellus, and Doig units. *AAPG Bull.*, **96**, 1099–1199.

Chepil, W.S. (1951) Properties of soil which influence wind erosion: IV. State of dry aggregate structure. *Soil Sci.*, **72**, 387–402.

Dagsson-Waldhauserová, P., **Arnalds, Ó.** and **Ólafsson, H.** (2017) Long-term dust aerosol production from natural sources in Iceland. *J. Air Waste Manag. Assoc.*, **67**(2), 173–181.

Dagsson-Waldhauserová, P., **Arnalds, Ó.** and **Ólafsson, H.** (2013) Long-term frequency and characteristics of dust storm events in Northeast Iceland (1949–2011). *Atmos. Environ.*, **77**, 117–127.

Dagsson-Waldhauserová, P., **Arnalds, Ó.**, **Ólafsson, H.**, **Skrabalova, L.**, **Sigurdardottir, G.M.**, **Branis, M.**, **Hladil, J.**, **Skala, R.**, **Navratil, T.**, **Chadimova, L.** and **Jonsdottir, I.** (2014a) Physical properties of suspended dust during moist and low wind conditions in Iceland. *Icel. Agric. Sci.*, **27**, 25–39.

Dagsson-Waldhauserová, P., **Arnalds, Ó.** and **Ólafsson, H.** (2014b) Long-term variability of dust events in Iceland (1949–2011). *Atmos. Chem. Phys.*, **14**, 13411–13422.

Dagsson-Waldhauserová, P., **Magnusdottir, A.Ö.**, **Ólafsson, H.** and **Arnalds, Ó.** (2016) The spatial variation of dust particulate matter concentrations during two Icelandic dust storms in 2015. *Atmosphere*, **7**, 77.

Del Bello, E., **Taddeucci, J.**, **Merrison, J.**, **Alois, S.**, **Iversen, J.** and **Scarlato, P.** (2018) Experimental simulations of volcanic ash resuspension by wind under the effects of atmospheric humidity. *Sci. Rep.*, **8**, 14509.

Đorđević, D., **Tošić, I.**, **Sakan, S.**, **Petrović, S.**, **Đuričić-Milanković, J.**, **Finger, D.C.** and **Dagsson-Waldhauserová, P.** (2019) Can volcanic dust suspended from surface soil and deserts of Iceland be transferred to central Balkan similarly to African Dust (Sahara)? *Front. Earth Sci.*, **7**, 142–154.

Drab, E., **Jaffrezo, A.** and **Colin, J.L.** (2002) Mineral particles content in recent snow at Summit (Greenland). *Atmos. Environ.*, **36**, 5365–5376.

Duce, R.A. (1995) Sources, distributions, and fluxes of mineral aerosols and their relationship to climates. In *Charlson, R.J., Heintzenberg, J. Eds.*, 43–72.

Einarsson, M.A. (1984) Climate of Iceland. In: *Climates of the Ocean* (Ed. van Loon, H.), Vol. **15**, pp. 673–697. Elsevier, Amsterdam, New York. Available at: https://raf hladan.is/bitstream/handle/10802/9550/Einarsson.pdf?se quence=1.

Formenti, P., **Schütz, L.**, **Balkanski, Y.**, **Desboeufs, K.**, **Ebert, M.**, **Kandler, K.**, **Petzold, A.**, **Scheuvens, D.**, **Weinbruch, S.** and **Zhang, D.** (2011) Recent progress in understanding physical and chemical properties of African and Asian mineral dust. *Atmos. Chem. Phys.*, **11**, 8231–8256.

Gislason, S.R., **Hassenkam, T.**, **Nedel, S.**, **Bovet, N.**, **Eiriksdottir, E.**, **Alfredsson, H.** and **Sigfusson, B.** (2011) Characterization of Eyjafjallajökull volcanic ash particles and a protocol for rapid risk assessment. *Atmos. Environ.*, **108**, 7307–7312.

Hillier, S. and **Marshall, J.** (1988) A rapid technique to make polished thin sections of sedimentary organic matter concentrates. *J. Sed. Res.*, **58**, 754–755.

Horwell, C.J. (2007) Grain size analysis of volcanic ash for the rapid assessment of respiratory health hazard. *J. Environ. Mon.*, **9**, 1107–1115.

Horwell, C.J., **Baxter, P.J.**, **Hillman, S.E.**, **Calkins, J.A.**, **Damby, D.E.**, **Delmelle, P.** and **Blond, J.S.L.** (2013) Physicochemical and toxicological profiling of ash from the 2010 and 2011 eruptions of Eyjafjallajökull and Grímsvötn volcanoes, Iceland using a rapid respiratory hazard assessment protocol. *Environ. Res.*, **127**, 63–73.

IUPAC (1994) Physical chemistry division commission on colloid and surface chemistry, subcommittee on characterization of porous solids: Recommendations for the characterization of porous solids. *Pure Appl. Chem.*, **66**, 1739–1758.

Johnson, B., **Turnbull, K.**, **Brown, P.**, **Burgess, R.**, **Dorsey, J.**, **Baran, A.**, **Webster, H.**, **Haywood, J.**, **Cotton, R.**, **Ulanowski, Z.** and **Hesse, E.** (2012) In situ observations of volcanic ash clouds from the FAAM aircraft during the eruption of Eyjafjallajökull in 2010. *J. Geophys. Res. Atmos.*, **117**(D20).

Kretz, R. (1980) Physical constants of minerals. In: *Handbook of Chemistry and Physics* (Ed., Weast, R. C.), 61st edn, pp. B-203–B-207. CRC Press, Boca Raton, FL.

Leadbetter, S.J., **Hort, M.C.**, **von Löwis, S.**, **Weber, K.** and **Witham, C.S.** (2012) Modeling the resuspension of ash deposited during the eruption of Eyjafjallajökull in spring 2010. *J. Geophy. Res.*, **117**, D00U10.

Meinander, O., **Dagsson-Waldhauserová, P.** and **Arnalds, Ó.** (2016) Icelandic volcanic dust can have a significant influence on the cryosphere in Greenland and elsewhere. *Polar Res.*, **35**, 31313.

Mockford, T., **Bullard, J.E.** and **Thorsteinsson, T.** (2018) The dynamic effects of sediment availability on the relationship between wind speed and dust concentration. *Earth Surf. Proces. Landform.*, **43**, 2484–2492.

Moroni, B., **Arnalds, Ó.**, **Dagsson-Waldhauserová, P.**, **Crocchianti, S.**, **Vivani, R.** and **Cappelletti, D.** (2018) Mineralogical and chemical records of Icelandic dust sources upon Ny-Ålesund (Svalbard Islands). *Front. Earth Sci.*, **6**, 187–219.

Navratil, T., **Hladil, J.**, **Strnad, L.**, **Koptikova, L.** and **Skala, R.** (2013) Volcanic ash particulate matter from the 2010 Eyjafjallajökull eruption in dust deposition at Prague, central Europe. *Aeol. Res.*, **9**, 191–202.

Oberdörster, G. (2001) Pulmonary effects of inhaled ultrafine particles. *Int. Arch. Occup. Environ. Health*, **74**, 1–8.

Olsson, J., **Stipp, S.L.S.**, **Dalby, K.N.** and **Gislason, S.R.** (2013) Rapid release of metal salts and nutrients from the 2011 Grímsvötn, Iceland volcanic ash. *Geochim. Cosmochim. Acta*, **123**, 134–149.

Prospero, M.J., **Bullard, J.E.** and **Hogkins, R.** (2012) High latitude dust over the North Atlantic: inputs from Icelandic proglacial dust storms. *Science*, **335**, 1078–1082.

Pye, K. (1987) *Aeolian Dust and Dust Deposits*. Academic Press Inc., London.

Quantachrome (2008) Autosorb-1/ASWin operating manual: Boynton Beach, Florida, Quantachrome Instruments, 161.

Richards-Thomas, T. and **McKenna-Neuman, C.** (2020) Laboratory investigation of particle-scale factors affecting the settling velocity of volcaniclastic dust. *J. Geophys. Res. Atmos.*, **125**, e2020JD032660.

Riley, N.A., **Rose, W.I.** and **Bluth, G.J.S.** (2003) Quantitative shape measurements of distal volcanic ash. *J. Geophy. Res.*, **108**(B10), 2504.

Robock, A. (2000) Volcanic eruptions and climate. *Geophys. Mono. Ser.*, **38**, 191–219.

Schumann, U.B., **Weinzierl, O.**, **Reitebuch, H.**, **Schlager, A.**, **Minikin, C.**, **Forster, C.**, **Baumann, R.**, **Sailer, T.**, **Graf, K.**, **Mannstein, H.** and **Voigt, C.** (2011) Airborne observations of the Eyjafjallajökull volcano ash cloud over Europe during air space closure in April and May 2010. Atmospheric Chemistry & Physics.

Smith, K.T. and **Dugmore, A.J.** (2006) Jökulhlaups circa Landnám: mid- to late first Millennium AD floods in south iceland and their implications for landscapes of settlement. *Geograf. Annal. Ser. A Phys. Geogr.*, **88**, 165–176.

Stevenson, J., **Loughlin, S.**, **Rae, C.**, **Thordarson, T.**, **Milodowski, A.**, **Gilbert, J.**, **Harangi, S.**, **Lukács, R.**, **Højgaard, B.**, **Árting, U.** and **Pyne- O'Donnell, S.** (2012) Distal deposition of tephra from the Eyjafjallajökull 2010 summit eruption. *J. Geophy. Res. Solid. Earth*, **117**(B9), B00C10.

Stohl, A., **Prata, A.**, **Eckhardt, S.**, **Clarisse, L.**, **Durant, A.**, **Henne, S.**, **Kristiansen, N.**, **Minikin, A.**, **Schumann, U.**, **Seibert, P.** and **Stebel, K.** (2011) Determination of time-and height-resolved volcanic ash emissions and their use for quantitative ash dispersion modeling: the 2010 Eyjafjallajökull eruption. *Atmos. Chem. Phys.*, **11**, 4333–4351.

Thorsteinsson, T., **Gísladóttir, G.**, **Bullard, J.** and **McTainsh, G.** (2011) Dust storm contributions to airborne particulate matter in Reykjavík, Iceland . *Atmos. Environ.*, **45**, 5924–5933.

Thorsteinsson, T., **Jóhannsson, T.**, **Stohl, A.** and **Kristiansen, N.I.** (2012) High levels of particulate matter in Iceland due to direct ash emissions by the Eyjafjallajökull eruption and resuspension of deposited ash. *J. Geophys. Res. Solid Earth*, **117**, 5.

Urupina, D., **Lasne, J.**, **Romanias, M.N.**, **Thiery, V.**, **Dagsson-Waldhauserova, P.** and **Thevenet, F.** (2019) Uptake and surface chemistry of SO2 on natural volcanic dusts. *Atmos. Environ.*, **217**, 116942.

Webb, P. and **Orr, C.** (1997) *Analytical Methods in Fine Particle Technology*. Micromeritics Instrument Corporation, Norcross, GA.

Wiegner, M., **Gasteiger, J.**, **Groβ, S.**, **Schnell, F.**, **Freudenthaler, V.** and **Forkel, R.** (2012) Characterization of the Eyjafjallajökull ash-plume: potential of lidar remote sensing. *Phys. Chem. Earth*, **45**, 76–86.

Wittmann, M., **Groot Zwaaftink, C.D.**, **Steffensen Schmidt, L.**, **Guðmundsson, S.**, **Pálsson, F.**, **Arnalds, Ó.**, **Björnsson, H.**, **Thorsteinsson, T.** and **Stohl, A.** (2017) Impact of dust deposition on the albedo of Vatnajökull ice cap, Iceland. *Cryosphere*, **11**, 741–754.

Y. León, C. (1998) New perspectives in mercury porosimetry. *Adv. Coll. Interface Sci.*, **76–77**, 341–372.

Manuscript received 8 March 2020; revision 22 October 2020; revision accepted 30 October 2020